

A Novel Meshless Method Based on the Virtual Construction of Node Control Domains for Porous Flow Problems

Xiang Rao^{1, 2, 3*}

¹School of Petroleum Engineering, Yangtze University, Wuhan 430100, P. R. China

²Key Laboratory of Drilling and Production Engineering for Oil and Gas, Hubei Province, Wuhan Hubei China, 430100, P. R. China

³Cooperative Innovation Center of Unconventional Oil and Gas (Ministry of Education & Hubei Province), Yangtze University, Wuhan, 430100, P. R. China

*Corresponding author: raoxiang0103@163.com, raoxiang0103@yangtzeu.edu.cn

Abstract: In this paper, a novel meshless method satisfying local mass conservation is developed by virtually constructing the node control domains. By defining the connectable node cloud, this novel meshless method uses the integral of the diffusion term and generalized difference operators to calculate the node control volumes by ensuring the local mass conservation. This novel method only focuses on the volume of the node control domain rather than the specific shape, so the construction of node control domains is called virtual, which will not increase the computational cost. To our knowledge, this is the first time to construct node control volumes in the meshless framework, so this novel method is named a node control domains-based meshless method, abbreviated as NCDMM, which can also be regarded as an extended finite volume method (EFVM). Taking two-phase porous flow problems as an example, the NCDMM discrete schemes meeting the local mass conservation are derived by integrating the generalized finite difference schemes of governing equations at each node control volume. Finally, existing commonly used low-order finite volume method (FVM) based nonlinear solvers for various porous flow models can be directly employed in the proposed NCDMM, significantly facilitating the general-purpose applications of the NCDMM. Theoretically, the proposed NCDMM has the advantages of previous meshless methods for discretizing computational domains with complex geometries, as well as the advantages of traditional low-order FVMs for stably handling a variety of porous flow problems with local mass conservation. Three numerical cases are implemented to test the computational accuracy, efficiency, convergence, and good adaptability to the calculation domain with complex geometry and complex boundary conditions.

Keywords: Meshless methods; Porous flow problems; Node control volume; Local mass conservation; Complex Geometry.

1. Introduction

Up to now, numerical methods are mainly divided into mesh-based and meshless types according to the discretization of the computational domain. For reservoir porous flow problems, due to the large size of the computational domain high-resolution methods are rarely applied, while the mesh-based low-order FVM is the most widely used. The significant factor limiting the mesh-based numerical methods is to generate a high-quality mesh to discretize the computational domain with complex geometry. Under this background, various meshless methods are proposed to obtain the high-accuracy calculation by only utilizing a node cloud instead of the mesh to discretize the calculation domain. However, due to the lack of the node control volume in previous meshless methods, less attention is paid to the local mass conservation, which is important in fluid flow simulation, so previous meshless methods still do not occupy a sufficient share in flow problems, especially in reservoir numerical simulation.

The generalized finite difference method (GFDM) is a popular domain-type meshless method [1, 2, 3]. This method uses a node cloud to discretize the computational domain and divides it into intersecting node influence subdomains. The spatial derivatives of functions in the governing equation can be expressed as the difference scheme of nodal values using the local Taylor expansion of multivariate functions and the weighted least square method in the subdomain, overcoming the mesh dependence of the traditional finite difference method (FDM). Up to now, this method has been widely used to solve seismic wave propagation problem [4], Burgers' equations [5, 6], shallow water equations [7, 8], problems of plates [9], heat conduction analysis [10, 11], elasticity problems [12, 13, 14], water wave interactions problems [15], soil mechanics [16, 17], flow problems [18, 19, 20, 21, 22], liquid-vapor phase transitions [23], and various scientific and engineering problems [24, 25, 26]. Rao et al. [27, 28] introduced the single point upstream (SPU) scheme [29, 30] in reservoir simulators to handle the convection term in the flow governing equations with a stable upwind effect and applied the upwind GFDM to solve the heat and mass transfer and two-phase porous flow problems. The good computational performances suggest that the upwind GFDM can realize high-quality meshless solutions to porous flow problems, and has great potential in the porous flow and reservoir numerical modeling.

For the reservoir flow problems, there are often point source terms (e.g. production and injection wells) in the reservoir domain [31], because the radius of the drilling wells is very small compared with the size of the reservoir domain. In the traditional FDM for reservoir numerical simulation [32, 33], the singular source term can be approximated by the nonsingular average source strength in the grid volume which contains the point source. The singular Dirac function representing the point sources is integrated to become nonsingular in the finite element method (FEM) [34, 35] and FVM [36, 37, 38, 39], thus the singular source or sink term is handled naturally. The low-order FVM is most widely used in reservoir numerical simulation, including the commonly used reservoir numerical simulation platforms CMG, ECLIPSE, AD-GPRS [40, 41], Matlab Reservoir Simulator Toolbox (MRST) [42] because it can adapt to wider mesh types than FDM, meet local mass conservation, and have simpler implementation for multiphase/multicomponent flow compared with FEM. However, FVM can directly deal with closed boundary conditions, but it struggles with more complex boundary conditions. For the computational domain with complex geometry (complex boundary geometry, fractures, caves, flow barriers, etc.), the generation of high-quality mesh is often difficult.

GFDM can give a high-accuracy generalized difference scheme satisfying local Taylor expansion and moving least squares when only using a node cloud to discretize the calculation domain, which motivates us to develop a meshless numerical simulation method that can flexibly discretize the calculation domains with complex geometry and handle complex boundary conditions. However, because the node cloud in previous meshless methods (including GFDM) lacks geometric information like node control volume, making it difficult to efficiently deal with singular source terms like production and injection wells and be coupled with the existing nonlinear solver of various porous flow models. Therefore, by introducing node control volumes to the meshless point cloud, this study aims to develop a node control domain-based meshless method (NCDMM) that satisfies local mass conservation and can handle singular source terms. Theoretically, the proposed NCDMM has the advantages of previous meshless methods for discretizing computational domains with complex geometries, as well as the advantages of traditional low-order FVMs for stably handling a variety of porous flow problems with local mass conservation and existing nonlinear solvers. Therefore, the proposed NCDMM is expected to become a new mainstream numerical method and provide a novel effective meshless tool to handle various scientific and engineering problems, especially reservoir flow problems.

This paper is organized as follows. Section 2.1 first briefly reviews the basic idea of GFDM. Section 2.2 gives the virtual construction method of node control domains, including the definitions of the node control domain and the connectable point cloud, and derivation of the calculation formula of node control volumes in

case of the connectable point cloud. Section 2.3 presents the NCDMM discrete scheme by integrating the GFDM discrete scheme on the node control domain and shows this method satisfies the local mass conservation. Section 2.4 shows the treatment of various boundary conditions. Section 2.5 conducts a convergence analysis of NCDMM. In Section 3, three numerical test cases are implemented to analyze the computational performances of the proposed NCDMM. The main conclusions are summarized in Section 4. Some future work is given in Section 5.

2. Methods

2.1 A brief review of GFDM

GFDM is a meshless method, that only uses a point cloud to discretize the computational domain. In GFDM, a node influence domain for each node is defined, and the influence domains of different nodes may intersect, i.e., $\Omega = \bigcup_i I_i$, where, Ω is the calculation domain and I_i is the influence domain of node i .

Let node i be a node in the calculation domain Ω , and the coordinate is (x_i, y_i) . The influence domain I_i of node i contains another n_i nodes except the node i , which are denoted as j ($j=1, 2, 3 \dots n_i$), and corresponding coordinates are (x_j, y_j) ($j=1, 2, 3 \dots n_i$). Taylor expansion of the unknown function at the node i is used to obtain:

$$u(x_j, y_j) = u(x_i, y_i) + \Delta x_j \left. \frac{\partial u}{\partial x} \right|_i + \Delta y_j \left. \frac{\partial u}{\partial y} \right|_i + \frac{1}{2} \left((\Delta x_j)^2 \left. \frac{\partial^2 u}{\partial x^2} \right|_i + 2\Delta x_j \Delta y_j \left. \frac{\partial^2 u}{\partial x \partial y} \right|_i + (\Delta y_j)^2 \left. \frac{\partial^2 u}{\partial y^2} \right|_i \right) + o(r^3) \quad (1)$$

where $\Delta x_j = x_j - x_i$, $\Delta y_j = y_j - y_i$.

$$\text{Simply denote } u_i = (x_i, y_i), \quad u_{x,i} = \left. \frac{\partial u}{\partial x} \right|_i, \quad u_{y,i} = \left. \frac{\partial u}{\partial y} \right|_i, \quad u_{xx,i} = \left. \frac{\partial^2 u}{\partial x^2} \right|_i, \quad u_{xy,i} = \left. \frac{\partial^2 u}{\partial x \partial y} \right|_i, \quad u_{yy,i} = \left. \frac{\partial^2 u}{\partial y^2} \right|_i.$$

Define the weighted error function $B(\mathbf{D}_u)$:

$$B(\mathbf{D}_u) = \sum_{j=1}^n \left[\left(u_i - u_j + \Delta x_j u_{x,i} + \Delta y_j u_{y,i} + \frac{1}{2} (\Delta x_j)^2 u_{xx,i} + \frac{1}{2} (\Delta y_j)^2 u_{yy,i} + \Delta x_j \Delta y_j u_{xy,i} \right) \omega_j \right]^2 \quad (2)$$

where $\mathbf{D}_u = (u_{x,i}, u_{y,i}, u_{xx,i}, u_{yy,i}, u_{xy,i})^T$, $\omega_j = \omega(\Delta x_j, \Delta y_j)$ is the weight function. Commonly used weight functions include exponential functions, potential functions, cubic splines, quartic splines, etc. [43]. Benito et al., [1], Gavete et al., [3], and Chen et al. [19] demonstrated that different weight-function types have little impact on the calculation results, and quartic spline function in Eq. (3) is generally used.

$$\omega_j = \begin{cases} 1 - 6 \left(\frac{r_j}{r_m} \right)^2 + 8 \left(\frac{r_j}{r_m} \right)^3 - 3 \left(\frac{r_j}{r_m} \right)^4 & r_j \leq r_m \\ 0 & r_j > r_m \end{cases} \quad (3)$$

where r_j is the Euclidean distance from node j to the central node i , and r_m is the radius of the influence domain of node i .

To minimize the error function, then the partial derivative of each component of the independent variable is equal to zero, that is,

$$\frac{\partial B(\mathbf{D}_u)}{\partial u_{x,i}} = 0, \frac{\partial B(\mathbf{D}_u)}{\partial u_{y,i}} = 0, \frac{\partial B(\mathbf{D}_u)}{\partial u_{xx,i}} = 0, \frac{\partial B(\mathbf{D}_u)}{\partial u_{yy,i}} = 0, \frac{\partial B(\mathbf{D}_u)}{\partial u_{xy,i}} = 0 \quad (4)$$

Eq. (4) are sorted into linear equations as follows:

$$\mathbf{A} \mathbf{D}_u = \mathbf{b} \quad (5)$$

where $\mathbf{A} = \mathbf{L}^T \boldsymbol{\omega} \mathbf{L}$, $\mathbf{b} = \mathbf{L}^T \boldsymbol{\omega} \mathbf{U}$, $\mathbf{L} = (\mathbf{L}_1^T, \mathbf{L}_2^T, \dots, \mathbf{L}_n^T)^T$, $\mathbf{L}_i = \left(\Delta x_i, \Delta y_i, \frac{\Delta x_i^2}{2}, \frac{\Delta y_i^2}{2}, \Delta x_i \Delta y_i \right)$,

$\boldsymbol{\omega} = \text{diag}(\omega_1^2, \omega_2^2, \dots, \omega_n^2)$, $\mathbf{U} = (u_1 - u_i, u_2 - u_i, \dots, u_n - u_i)^T$.

Then, Eq. (5) can be rewritten as:

$$\mathbf{D}_u = (u_{x,i}, u_{y,i}, u_{xx,i}, u_{yy,i}, u_{xy,i})^T = \mathbf{A}^{-1} \mathbf{b} = \mathbf{A}^{-1} \mathbf{L}^T \boldsymbol{\omega} \mathbf{U} = \mathbf{M} \mathbf{U} \quad (6)$$

where $\mathbf{M} = \mathbf{A}^{-1} \mathbf{L}^T \boldsymbol{\omega}$.

For the convenience of representation, the elements of the matrix \mathbf{M} are denoted as m_{kj}^i , where the superscript i indicates that the matrix \mathbf{M} is calculated based on the influence domain of node i .

From the matrix \mathbf{M} , it is not difficult to obtain the approximate expressions of spatial derivatives of the unknown function at the central node i :

$$\begin{aligned} \frac{\partial u}{\partial x}|_i &= \sum_{j=1}^{n_i} m_{1j}^i (u_j - u_i), \quad \frac{\partial u}{\partial y}|_i = \sum_{j=1}^n m_{2j}^i (u_j - u_i), \quad \frac{\partial^2 u}{\partial x^2}|_i = \sum_{j=1}^n m_{3j}^i (u_j - u_i), \\ \frac{\partial^2 u}{\partial y^2}|_i &= \sum_{j=1}^n m_{4j}^i (u_j - u_i), \quad \frac{\partial^2 u}{\partial x \partial y}|_i = \sum_{j=1}^n m_{5j}^i (u_j - u_i) \end{aligned} \quad (7)$$

2.2 Virtual construction of node control domains

Although meshless GFDM has been widely used in various scientific and engineering problems, when there are singular Dirac function terms such as the point source in the equation, because no integration treatment is used in GFDM, it is difficult to integrate the singular Dirac term like FEM and FVM to eliminate the singularity in the governing equation. In the traditional FDM for reservoir numerical simulation, each node has a corresponding grid, so the control volume of each node is the volume of the corresponding grid, so the strength of the singular point source can be approximated by the average source strength of the unit grid volume. It can be predicted that this processing method has good convergence, because the smaller the grid volume is, the closer the average source strength of the unit grid volume in FDM is to the real strength of the singular point source. However, as a meshless method, GFDM only has the concept of node but does not have the concept of grid volume. It is difficult to approximate the singular point source to the nonsingular grid average source term as FDM. Therefore, it is difficult to apply GFDM to the flow problem with point sources. In the field of subsurface porous flow, especially in reservoir numerical simulation, because there will be injection and production wells whose scale is much smaller than the reservoir scale in the reservoir calculation domain, point sources often exist. To solve this problem, this paper attempts to define the concept of node control volume in GFDM for the first time to deal with the point source term and form a node control volume-based meshless method.

Def. 1: We define that each node has its control domain in addition to its influence domain, and the control domains of different nodes do not intersect each other, which meets:

$$\Omega = \bigcup_i \Omega_i, \quad \Omega_i \cap \Omega_j = \emptyset \quad (8)$$

$$\sum_{i=1}^{n_p} V_i = V_\Omega \quad (9)$$

where Ω_i is the control domain of node i , V_i is the volume of the domain Ω_i , named the control volume of node i , V_Ω is the volume of the calculation domain Ω , and n_p is the total number of nodes in the calculation domain. Of course, due to the possible complex node distribution of the point cloud discretizing the computational domain, the geometric shape of the node control domain Ω_i can not be described explicitly, but this paper only cares about the volume V_i of the corresponding node control domain, without figuring out the specific shape of the node control domain, this is why it is called virtual construction.

Def. 2: Then, we define that, the node cloud of the computational domain is called connectable means that for any two nodes in the point cloud (may as well suppose as node i and node j), if there is node j in the influence domain of node i , there must also be node i in the influence domain of node j .

In fact, the connectable point cloud is easy to satisfy. For example, to set the size of the influence domain of each node to be the same. Of course, the methods of constructing connectable point clouds can be diverse.

Def. 3: In the case of the connectable point cloud of the computational domain, if j is in the influence domain of node i , we denote that i is neighboring to j , and j is neighboring to i , and (i, j) is a neighboring pair.

Assuming the point cloud of the computational domain is connectable, for any node i , by integrating Δu at node i in the node control domain Ω_i , we can approximately obtain

$$\int_{\Omega_i} \Delta u d\Omega \approx V_i \Delta u \approx V_i \sum_{j=1}^n (m_{3j}^i + m_{4j}^i) (u_j - u_i) \quad (10)$$

According to the Gauss formula, it is obtained that

$$\int_{\Omega_i} \Delta u d\Omega \approx \int_{\Omega_i} \nabla \cdot (\nabla u) d\Omega \approx \int_{\partial\Omega_i} \nabla u \cdot \bar{n} d\Omega \approx \sum_{j=1}^n \int_{\partial\Omega_i \cap \partial\Omega_j} \nabla u \cdot \bar{n} d\Omega \quad (11)$$

where $\partial\Omega_i$ and $\partial\Omega_j$ are the boundaries of Ω_i and Ω_j respectively, $\partial\Omega_i \cap \partial\Omega_j$ are the common boundary of Ω_i and Ω_j , \bar{n} is the external normal vectors of pairs, then we think that they are only related to u_i and u_j . Therefore, by an analogy between Eq. (10) and Eq. (11), it is obtained that:

$$\int_{\partial\Omega_i \cap \partial\Omega_j} \nabla u \cdot \bar{n} d\Omega = V_i (m_{3j}^i + m_{4j}^i) (u_j - u_i) \quad (12)$$

Because the point cloud is connectable, node i is also in the influence domain of node j . Similarly, when taking node j as the central node, it can be obtained that

$$\int_{\partial\Omega_i \cap \partial\Omega_j} \nabla u \cdot \bar{n}' d\Omega = V_j (m_{3i}^j + m_{4i}^j) (u_i - u_j) \quad (13)$$

There is $\bar{n}' = -\bar{n}$, so we obtain that

$$V_i (m_{3j}^i + m_{4j}^i) (u_j - u_i) = V_j (m_{3i}^j + m_{4i}^j) (u_j - u_i) \Leftrightarrow V_i (m_{3j}^i + m_{4j}^i) = V_j (m_{3i}^j + m_{4i}^j) \quad (14)$$

It should be noted that if node i or node j is a boundary node, Eq. (14) is often not satisfied. This is because there are nodes only on one side of the boundary, which results in the center of the local point cloud in the boundary node's influence domain being far away from that boundary node [27, 28, 44], i.e. the local point cloud is of low quality, making the accuracy of the generalized difference expressions in Eq. (7) for approximating the spatial derivatives of the unknown function. Thus, for the boundary node, $m_{3j}^i + m_{4j}^i < 0$ generally exists, while for the inner node, it can generally meet $m_{3i}^j + m_{4i}^j \geq 0$, Eq. (14) is valid unless the control volume of the boundary node is negative, which is unreasonable. For example, as shown in Fig. 1 (a), node 3 is a boundary node, and the radius of the influence domain is selected as $\sqrt{2} + 0.1$. At this time, if only nodes 2, 3, 4, 7, 8, and 9 are included in the influence domain of node 3, the linear equations in Eq. (6) are unsolvable such that Eq. (7) can not be obtained. This singular situation also brings trouble to the construction of a general calculation method of control volumes. As shown in Fig. 1 (b), when the influence domain of node 3 is further expanded to 2.1 to include other nodes 1, 5, and 13, the results can be calculated according to Eq. (6):

$$\Delta u = 6.1019 \times 10^{-6} (u_1 - u_3) + 1.0714 (u_2 - u_3) + 1.0714 (u_4 - u_3) + 6.1019 \times 10^{-6} (u_5 - u_3) + \\ -0.0714 (u_7 - u_3) - 1.8573 (u_8 - u_3) - 0.0714 (u_9 - u_3) + 1.0000 (u_{13} - u_3) \quad (15)$$

Thus, when the boundary node 3 is the central node, $m_{38}^3 + m_{48}^3 = -1.8573 < 0$. This example proves the above conclusion, which makes it difficult for us to calculate the node control volume according to Eq. (14).

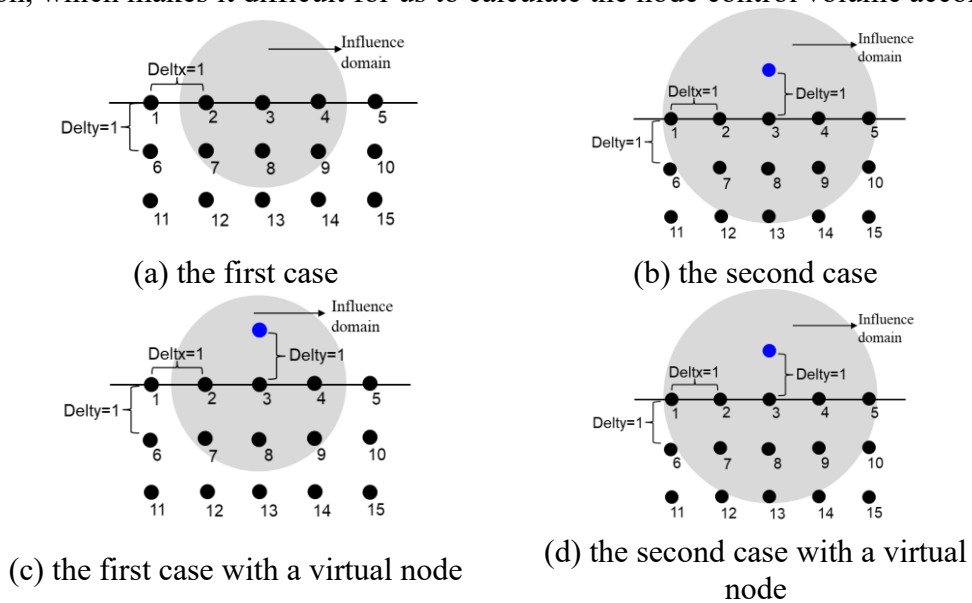


Fig. 1 The illustration of adding virtual nodes

We know that when dealing with derivative boundary conditions, GFDM can generally add a virtual node outside the calculation domain of derivative boundary nodes to improve the approximation accuracy of the generalized finite difference expressions of the spatial derivatives at boundary nodes in Eq. (7) [27, 28]. It

inspires us that when calculating the node control volume, to eliminate the problems caused by boundary nodes, virtual nodes corresponding to boundary nodes can be added outside the boundary of the whole calculation domain, so that for any boundary node i , $(m_{3j}^i + m_{4j}^i) \geq 0$ holds, and the problem that the linear equations in Eq. (6) are unsolvable and Eq. (7) cannot be obtained can be overcome. Still taking Fig. 1 as an example, we only add a virtual node M in the influence domain of node 3 in Fig. 1 (a) to obtain Fig. 1 (c) (in fact, two virtual nodes also need to be added outside boundary nodes 2 and 4. The illustration here is used to show that even if only one virtual node is added outside the concerned central node 3, it is sufficient to meet the requirement). In this case, using Eq. (6) it can be calculated as:

$$\begin{aligned} \Delta u = & 1.0000(u_M - u_3) + 0.9998(u_2 - u_3) + 0.9998(u_4 - u_3) + \\ & 1.7590 \times 10^{-4}(u_7 - u_3) + 0.9996(u_8 - u_3) + 1.7590 \times 10^{-4}(u_9 - u_3) \end{aligned} \quad (16)$$

It can be seen that linear equations in Eq. (6) after adding virtual nodes become solvable, and $m_{38}^3 + m_{48}^3 = 0.9996 > 0$ is obtained.

Similarly, in Fig. 1 (b), the virtual node m is also added to obtain Fig. 1 (d), which can be calculated as follows.

$$\begin{aligned} \Delta u = & 1.0000(u_M - u_3) + 4.8824 \times 10^{-6}(u_1 - u_3) + 0.8572(u_2 - u_3) + 1.0714(u_4 - u_3) \\ & + 4.8824 \times 10^{-6}(u_5 - u_3) + 0.1427(u_7 - u_3) + 0.7145(u_8 - u_3) + 0.1427(u_9 - u_3) \\ & + 4.4760 \times 10^{-6}(u_{13} - u_3) \end{aligned} \quad (17)$$

It can also be seen that, after adding virtual nodes outside the boundary node, it is obtained that $m_{38}^3 + m_{48}^3 = 0.7145 > 0$.

In addition, it should also be noted that, after adding a virtual node outside the boundary node, the control domain in Eq. (14) of the boundary node will not be completely included in the calculation domain. At this time, Eq. (14) needs to be modified as follows:

$$V_i(m_{3j}^i + m_{4j}^i) = V_j(m_{3i}^j + m_{4i}^j) \quad (18)$$

where V_i is the control volume of each node after adding virtual nodes on the boundary, rather than the node control volume \bar{V}_i only inside the calculation domain.

Def. 4: Then, we introduce the concept of feature angle at nodes to establish the relationship between V_i and \bar{V}_i . The characteristic angle at the node introduced in this paper is the same as that defined at the node in the boundary element method (BEM). For the smooth node on the boundary shown in Fig. 2 (a), the characteristic angle is generally π , for the corner node on the boundary shown in Fig. 2 (b), the characteristic angle is the included angle θ of tangents on both sides, and for the internal nodes in the calculation domain, the characteristic angle of the node is 2π . Therefore, supposing that node i is a boundary node and θ_i is the characteristic angle of the node, it is obtained that:

$$\bar{V}_i = \frac{\theta_i}{2\pi} V_i \quad (19)$$

Thus, Eq. (9) is rewritten as:

$$\sum_{i=1}^{n_p} \frac{\theta_i}{2\pi} V_i = V_\Omega \quad (20)$$

Finally, if there are n_c pairs of i - j , there is an Eq. (18) for each pair of i - j . combined with Eq. (20), $n_c + 1$ linear equations can be obtained, and there are n_p unknown node control volumes, and $n_c > n_p$ generally holds. Therefore, Eq. (18) and Eq. (20) form an overdetermined linear equation system, which can be solved via the least square method, and then calculated \bar{V}_i by using Eq. (19). Note that the above derivation process has a premise assumption, that is, the point cloud of the computational domain is connectable. In addition, another detail needs to explain. Since Eq. (18) and Eq. (20) form an overdetermined system of equations, which is solved by minimizing the residue in the 2-norm of the equations, Eq. (20) may not be strictly satisfied. However, the sum of the control volume of each node is equal to the total volume of the calculation domain, which is the key to the mass conservation of the calculation domain. Therefore, Eq. (20) is required to be strictly satisfied. Therefore, this paper uses the "large number method" to multiply both sides of Eq. (20) by a

larger number G . Generally, the order of magnitude of G is about 4 orders of magnitude larger than that of the node control volume, that is, Eq. (20) is modified as:

$$G \sum_{i=1}^{n_p} \frac{\theta_i}{2\pi} V_i = G V_\Omega \quad (21)$$

We illustrate the reasonability of the above calculation method of node control volumes with a ‘naïve’ case where simple Cartesian node collocation is used. As shown in Fig. 2, it is a rectangular calculation domain $[0, 20] \times [0, 20]$, using 3×3 uniformly distributed nodes and virtual nodes are added outside the boundary of the calculation domain. May as well select the radius of the influence domain as $10\sqrt{2} + 0.1$, and then it can be obtained that the distribution geometry in the influence domain of each internal or boundary node is the same and symmetrical. Therefore, for any adjacent i - j pair, $(m_{3j}^i + m_{4j}^i) = (m_{3i}^j + m_{4i}^j)$ holds. Then according to Eq.

(17), $\forall i, j, V_i = V_j$ holds. For the nodes at the four corners of the calculation domain, there is $\theta_i = \frac{\pi}{2}$ ($i = 1, 3, 7, 9$), For the nodes at the midpoint of the four edges of the calculation domain, there is $\theta_i = \pi$ ($i = 2, 4, 6, 8$), and for the internal nodes of the calculation domain, there is $\theta_i = 2\pi$ ($i = 5$), to obtain:

$$\begin{aligned} \sum_{i=1}^{n_p} \frac{\theta_i}{2\pi} V_i &= 4 \times \frac{1}{4} V_5 + 4 \times \frac{1}{2} V_5 + V_5 = 20 \times 20 \Rightarrow V_i = 100 \Rightarrow \bar{V}_5 = 100 \\ &\Rightarrow \bar{V}_1 = \bar{V}_3 = \bar{V}_7 = \bar{V}_9 = 25, \bar{V}_2 = \bar{V}_4 = \bar{V}_6 = \bar{V}_8 = 50 \end{aligned} \quad (22)$$

The above-calculated node control volumes are matched with the grid volumes in the Cartesian grid corresponding to the uniformly distributed nodes, which shows the reasonability of the above definition and calculation method of the node control volume.

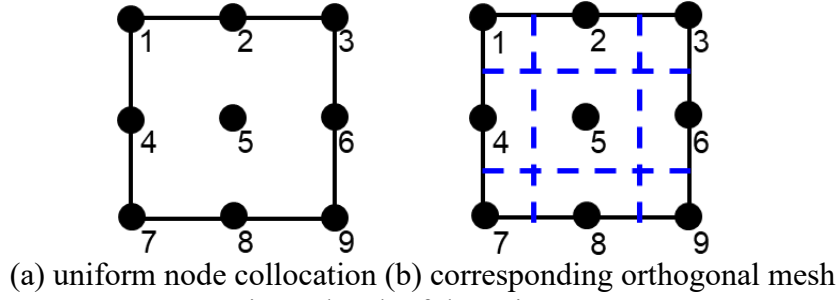


Fig. 2 sketch of the naive case

From the above process, we can predict that the introduced node control volume in GFDM is related not only to the node coordinates of the point cloud but also to the size of the influence domain (i.e. i - j pairs between nodes), which is expressed in the form of abstract function as follows:

$$V_i = f(X, C) \quad (23)$$

where X is the information of nodes' coordinates in the calculation domain and C is information of the i - j pairs in the calculation domain. This is also easy to understand because the X and C information in GFDM can correspond to the mesh center and mesh neighboring relationship in the traditional mesh system, while the mesh center and mesh neighboring relationship in the traditional mesh system uniquely determine the mesh volume. Correspondingly, in the meshless system, the node control volume is uniquely determined by X and C . In the numerical test cases in Section 3, we will show that different influence domain radii will yield different node control volumes.

It should be specially pointed out that when calculating the node control volume, the radius of the node influence domain cannot be too large, because when the node influence domain is too large, there will be many nodes in the influence domain, which will bring three problems:

- (i) The dimension of the overdetermined equations is large, which reduces the calculation efficiency;
- (ii) Rao et al. [27, 28] pointed out that, for convection-dominated heat and mass transfer and multiphase flow problems, the large radius of the influence domain will reduce the quality of node distribution in the influence domain of the nodes at or near the boundary, causing the decrease of the approximation accuracy of the generalized difference operator. In addition, the large radius of the influence domain will also increase the dissipation error of the single point upwind (SPU) scheme used for discretization of the convection term.
- (iii) The connection between nodes is more complex, resulting in a large bandwidth of the Jacobian matrix in

the Newton-iteration-based nonlinear solver, which will increase the computational cost of the linear solver.

2.3 NCDMM discrete scheme of governing equations

This paper takes the two-phase porous flow equations in Eq. (24) and Eq. (25) as an example to illustrate the specific NCDMM-based discrete scheme.

$$\nabla \cdot \left(\frac{kk_{ra}}{B_a \mu_a} \nabla p_a \right) + q_{a,well} = \frac{\partial}{\partial t} \left(\frac{\phi S_a}{B_a} \right) \quad (24)$$

where k is the permeability, $a = o$ or w , which denotes oil phase or water phase; $k_{ra} = k_{ra}(S_w)$ are the relative permeability of phase a ; B_a is the volume coefficient of the phase a ; μ_a is the viscosity of phase a ; p_a is the pressure of phase a ; t is time; S_a is the saturation of phase a , which meets $S_o + S_w = 1$; $\phi = \phi(p)$ is the porosity which is a function of the pressure. $q_{a,well}$ is the strength of the source or sink of phase a from production or injection wells.

Assuming that the node pressure and water saturation at time t are known, integrate both sides of Eq. (24) on the node control volume of node i , and take the implicit scheme for each physical quantity, that is, the value of time $t + \Delta t$. The approximation of the integration of the first term on the left side of Eq. (24) is as follows:

$$\int_{V_i} \nabla \cdot \left(\frac{kk_{ra}}{B_a \mu_a} \nabla p_a \right) d\Omega = \int_{V_i} \sum_{j=1}^{n_i} \left[\frac{k_{ij}^{t+\Delta t} k_{ra,ij}^{t+\Delta t}}{B_{a,ij}^{t+\Delta t} \mu_{a,ij}^{t+\Delta t}} (m_{3,j}^i + m_{4,j}^i) (p_{a,(i,j)}^{t+\Delta t} - p_{a,i}^{t+\Delta t}) \right] d\Omega \quad (25)$$

in which, it should be emphasized that n_i is the number of real nodes in the influence domain of node i , (i, j) refers to the sequence number in all nodes of the j -th real node in the influence domain of node i except node i itself. The single-point upstream scheme in Eq. (26) is used for relative permeability to handle the convection term stably [27, 28], the harmonic average scheme in Eq. (27) is used for permeability, and the arithmetic average scheme in Eq. (28) is used for phase volume coefficient and viscosity, respectively.

$$k_{ra,ij}^{t+\Delta t} = \begin{cases} k_{ra,i}(S_{w,i}^{t+\Delta t}) & \text{if } p_{a,(i,j)}^{t+\Delta t} \geq p_{a,i}^{t+\Delta t} \\ k_{ra,i}(S_{w,i}^{t+\Delta t}) & \text{if } p_{a,(i,j)}^{t+\Delta t} < p_{a,i}^{t+\Delta t} \end{cases}, a = o \text{ or } w \quad (26)$$

$$k_{ij}^{t+\Delta t} = \frac{2}{1/k_i^{t+\Delta t} + 1/k_j^{t+\Delta t}} \quad (27)$$

$$B_{a,ij}^{t+\Delta t} = \frac{B_{a,i}^{t+\Delta t} + B_{a,j}^{t+\Delta t}}{2}, \quad \mu_{a,ij}^{t+\Delta t} = \frac{\mu_{a,i}^{t+\Delta t} + \mu_{a,j}^{t+\Delta t}}{2}, \quad a = o \text{ or } w \quad (28)$$

Eq. (25) can be further approximated as:

$$\int_{V_i} \nabla \cdot \left(\frac{kk_{ra}}{B_a \mu_a} \nabla p_a \right) d\Omega = \sum_{j=1}^{n_i} \left[\frac{k_{ij}^{t+\Delta t} k_{ra,ij}^{t+\Delta t}}{B_{a,ij}^{t+\Delta t} \mu_{a,ij}^{t+\Delta t}} V (m_{3,j}^i + m_{4,j}^i) (p_{a,(i,j)}^{t+\Delta t} - p_{a,i}^{t+\Delta t}) \right], a = o \text{ or } w \quad (29)$$

For the second term of the left side of Eq. (24), if there is no singular source or sink term (i.e. no production well or injection well) at node i , then:

$$\int_{V_i} q_{a,well} d\Omega = Q_{a,well} = 0, a = o \text{ or } w \quad (30)$$

If there are production wells or injection wells at node i , since the proposed NCDMM is essentially a meshless method, although the value of node control volume can be calculated in Section 2.2, it is difficult to describe the specific geometric shape of the node control domain. Therefore, in NCDMM, the well index is calculated as:

$$WI_i = \frac{2\pi k_i h_i}{\ln(r_{e,i}/r_w) + s}, \quad r_{e,i} = 0.14\sqrt{2V_i/h_i} \quad (31)$$

where $r_{e,i}$ is the equivalent radius, r_w is the well radius, and s is the skin factor.

If the well is a production well, then

$$\int_{V_i} q_{a,well} d\Omega = Q_{a,well} = \frac{k_{ra,if}^{t+\Delta t}}{B_{a,if}^{t+\Delta t} \mu_{a,if}^{t+\Delta t}} W I_i \left(p_{wf}^{t+\Delta t} - p_{a,i}^{t+\Delta t} \right), a = o \text{ or } w \quad (32)$$

If the well is a water injection well, then

$$\int_{V_i} q_{o,well} d\Omega = Q_{o,well} = 0 \quad (33)$$

$$\int_{V_i} q_{w,well} d\Omega = Q_{w,well} = \frac{1}{B_{w,if}^{t+\Delta t}} \left(\frac{k_{ro,if}^{t+\Delta t}}{\mu_{o,if}^{t+\Delta t}} + \frac{k_{rw,if}^{t+\Delta t}}{\mu_{w,if}^{t+\Delta t}} \right) W I_i \left(p_{wf}^{t+\Delta t} - p_{w,i}^{t+\Delta t} \right) \quad (34)$$

The integral of the term of the right side of Eq. (24) is approximated as:

$$\int_{V_i} \frac{\partial(\phi S_a)}{\partial t} d\Omega = \frac{V_i}{\Delta t} \left[\left(\frac{\phi_i^{t+\Delta t} S_{a,i}^{t+\Delta t}}{B_{a,i}^{t+\Delta t}} \right) - \left(\frac{\phi_i^t S_{a,i}^t}{B_{a,i}^t} \right) \right], a = o \text{ or } w \quad (35)$$

Based on the above results, the approximate expressions of Eq. (24) can be obtained as follows:

$$\sum_{j=1}^{n_i} \left[\frac{k_{ij}^{t+\Delta t} k_{ra,ij}^{t+\Delta t}}{B_{a,ij}^{t+\Delta t} \mu_{a,ij}^{t+\Delta t}} V_i \left(m_{3,j}^i + m_{4,j}^i \right) \left(p_{a,(i,j)}^{t+\Delta t} - p_{a,i}^{t+\Delta t} \right) \right] + Q_{a,well} = \frac{V_i}{\Delta t} \left[\left(\frac{\phi_i^{t+\Delta t} S_{a,i}^{t+\Delta t}}{B_{a,i}^{t+\Delta t}} \right) - \left(\frac{\phi_i^t S_{a,i}^t}{B_{a,i}^t} \right) \right] \quad (36)$$

To make direct use of the nonlinear solver in current reservoir numerical simulators based on FVM, the concept of transmissibility similar to that in the FVM-based discrete scheme can be extracted from the first item of the left side of Eq. (36), that is, when node i is considered (i.e. consider the influence domain of node i), transmissibility between node i and node j (in fact, it should be node (i, j) because (i, j) is the sequential number in all nodes of the j -th node in the influence domain of node i . Here denoted as j for simplicity of expression) is:

$$T_{i,ij}^{t+\Delta t} = \left[k_{ij}^{t+\Delta t} V_i \left(m_{3,j}^i + m_{4,j}^i \right) \right] \quad (37)$$

where i in the subscript i, ij means the transmissibility between node i and node j is obtained when the influence domain of node i is considered.

Similarly, when considering node j , we can obtain:

$$T_{j,ij}^{t+\Delta t} = \left[k_{ji}^{t+\Delta t} V_j \left(m_{3,i}^j + m_{4,i}^j \right) \right] \quad (38)$$

Due to the harmonic average scheme in Eq. (27) adopted for permeability in Eq. (38), comparing Eq. (37) with Eq. (38), it is obtained that

$$T_{i,ij}^{t+\Delta t} = T_{j,ij}^{t+\Delta t} \quad (39)$$

Eq. (39) shows that the proposed NCDMM satisfies the local mass conservation [45, 46, 47, 48], which is important in flow simulation, then the transmissibility can be uniformly written as:

$$T_{ij}^{t+\Delta t} = T_{i,ij}^{t+\Delta t} = T_{j,ij}^{t+\Delta t} = k_{ij}^{t+\Delta t} V_i \left(m_{3,j}^i + m_{4,j}^i \right) = k_{ji}^{t+\Delta t} V_j \left(m_{3,i}^j + m_{4,i}^j \right) \quad (40)$$

Then Eq. (36) can be further rewritten as

$$\sum_{j=1}^{n_i} \left[\frac{k_{ra,ij}^{t+\Delta t}}{B_{a,ij}^{t+\Delta t} \mu_{a,ij}^{t+\Delta t}} T_{ij}^{t+\Delta t} \left(p_{a,(i,j)}^{t+\Delta t} - p_{a,i}^{t+\Delta t} \right) \right] + Q_{a,well} = \frac{V_i}{\Delta t} \left[\left(\frac{\phi_i^{t+\Delta t} S_{a,i}^{t+\Delta t}}{B_{a,i}^{t+\Delta t}} \right) - \left(\frac{\phi_i^t S_{a,i}^t}{B_{a,i}^t} \right) \right] \quad (41)$$

From sections 2.2 and 2.3, it can be seen that the proposed NCDMM firstly introduces the basic concepts of node control volume and connectable collocation in GFDM, then obtains the NCDMM discrete scheme satisfying the local mass conservation by integrating the GFDM discrete scheme. Therefore, in essence, the proposed NCDMM is the integral form of GFDM in the case of connectable collocation.

2.4 Treatment of boundary conditions and construction of global equations

The proposed NCDMM is essentially the integral form of GFDM, but this integral form refers to the integral of the discretization scheme of the governing equation. For the boundary conditions, the treatment of NCDMM is the same as that of GFDM, so compared with the traditional FVM, NCDMM can directly handle more complex boundary conditions. When NCDMM deals with derivative boundary conditions, the virtual nodes added at the boundary node need to be used to improve the approximation accuracy of generalized finite difference operators for the spatial derivatives of unknown functions at the boundary node [27, 28, 44]. Fig. 3 is a sketch of the virtual node added at the derivative boundary node from the literature [27]. It can be seen that, when the blue virtual node is not added, the black nodes in the influence domain of the red boundary node are on the same side of the tangent at the boundary node. At this time, the position of the center of gravity

of all nodes in the boundary-node influence domain deviates much from that of the considered boundary node, such that the accuracy of the spatial derivatives of the unknown function given by Eq. (7) is low. After adding a blue virtual node in the influence domain of the boundary node, the accuracy of Eq. (7) for spatial derivatives will be significantly improved. Therefore, the virtual node corresponding to the derivative boundary node will also participate in the construction of the global equations. For details, please refer to the literature [27].

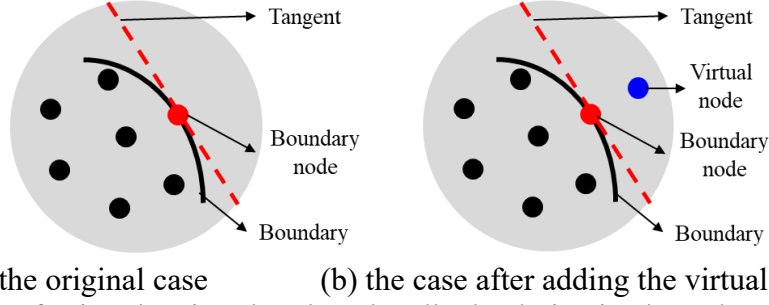


Fig. 3 Sketch of using the virtual node to handle the derivative boundary condition [27]

Taking the pressure function as an example, if a boundary node i satisfies the Dirichlet boundary conditions in Eq. (42), the discrete equations at node i are shown in Eq. (43):

$$p|_{\Gamma} = f(x, y), \quad S_w|_{\Gamma} = g(x, y) \quad (42)$$

$$p_{o,i} = f(x_i, y_i), \quad S_{w,i} = g(x_i, y_i) \quad (43)$$

where, x_i and y_i are the x coordinate and y coordinate of node i respectively.

Suppose a boundary node i satisfies the second-type (Neumann) boundary conditions, and the virtual node added for the treatment of the derivative boundary condition at node i is node j , then in the global equations, the equations at node i is the discrete schemes of the governing equations in Eq. (41). Corresponding to the Neumann boundary conditions in Eq. (44), the equations at node j are the discrete equations in Eq. (45).

$$\frac{\partial p}{\partial \mathbf{n}}|_{\Gamma} = f(x, y) \quad (44)$$

$$n_x \sum_{l=1}^{n_i} m_{1l}^i (p_{o,(i,l)} - p_{o,i}) + n_y \sum_{l=1}^{n_i} m_{2l}^i (p_{o,(i,l)} - p_{o,i}) = f(x_i, y_i) \quad (45)$$

where, n_x and n_y are the components of the external normal vector \mathbf{n} at the boundary node, and n_i is the number of nodes in the influence domain of node i other than node i itself (including virtual nodes). Since virtual node j is in the influence domain of node i , there is l such that $(i, l) = j$.

For the third type of boundary condition (e.g. the Robin-type boundary condition) which is also the derivative boundary condition, the treatment method is the same as that for Neumann boundary conditions.

Therefore, suppose there are n_m nodes in the calculation domain, including n_{1BC} nodes that meet the first-type (Dirichlet) boundary condition and n_{2BC} nodes that meet the derivative-type boundary condition, then the number of the virtual nodes involved in the construction of the global equations are also n_{2BC} , so the nodes involved in the construction of the global equations are n_m real nodes and the n_{2BC} virtual nodes corresponding to the nodes which meet the derivative-type boundary conditions. Among these nodes, for the n_m real nodes, the equations at the interior nodes and boundary nodes that meet the derivative boundary conditions are the discrete schemes in Eq. (41) of the governing equations, the equations corresponding to the nodes which meet the Dirichlet boundary condition are Eq. (43). For the n_{2BC} virtual nodes, the corresponding equations are the equations of the derivative boundary conditions in Eq. (45).

Therefore, there are only two types of equations in global equations, one is the Eq. (41) representing the NCDMM-based discrete governing equations, and the other is the Eq. (43) and the Eq. (45) representing the discrete boundary conditions. For the first type, the connectable point cloud in the calculation domain and the size of the influence domain of each node can be used to obtain all i - j neighboring pairs, which corresponds to the neighboring connections between cells in the traditional FVM. The control volume of each node can be calculated by Eq. (18) and Eq. (21), which corresponds to the volume of each cell in the traditional FVM, using Eq. (46) the transmissibility of each i - j pair can be calculated, which corresponds to the transmissibility of the connection between neighboring cells in the traditional FVM. The above three parameters (i - j neighboring pairs, node control volumes, and transmissibilities) in NCDMM are the required parameters in

the nonlinear solver for FVM-based reservoir numerical simulation. Therefore, the NCDMM discrete governing equations shown in Eq. (41) at the $n_m - n_{1BC} - n_{2BC}$ interior nodes and n_{2BC} derivative-boundary-condition nodes can be quickly constructed like the traditional FVM. Then, Eq. (45) representing the derivative boundary conditions are filled at the virtual nodes corresponding to the n_{2BC} derivative-boundary-condition nodes, and finally, the equations shown in Eq. (43) are added to the Dirichlet-boundary-condition nodes. Of course, if the bottom hole pressure (BHP) needs to be calculated, the equation of well production rates and BHP needs to be added. The nonlinear solver in the FVM-based simulator can be employed to solve the formed global equations. It can be seen that, Eqs. (43) and (45) representing the boundary conditions are generally linear. Therefore, compared with the traditional FVM, the proposed NCDMM does not increase the nonlinearity of the equations, so it can be expected, that the computational efficiency of the proposed NCDMM is comparable to that of traditional FVM. The numerical examples in Section 3 will prove this assertion with specific data. Note that, when it is the most common closed boundary condition in reservoir simulation, the discrete equation of the boundary condition is not required, but only the connection table composed of the connection between the nodes and the corresponding transmissibility is constructed without considering the connection between the boundary nodes and the virtual nodes in the first item on the left of the discrete scheme in Eq. (41) of flow governing equations at the boundary nodes. In this case, the virtual boundary nodes are only used as geometric entities to help calculate the node control volumes and the transmissibility of connections between the boundary node and its neighboring real nodes, and there is not any physical quantity at the virtual nodes that need to be solved.

2.5 Convergence analysis of NCDMM

We know that the traditional FDM has low-order accuracy, that is, the convergence order is less than or equal to 2, as shown in Fig. 4 (a), node 0 is the central node, with $\Delta x_1 = -\Delta x$ and $\Delta y_1 = 0$ for node 1, $\Delta x_2 = \Delta x$ and $\Delta y_2 = 0$ for node 2, $\Delta x_3 = 0$ and $\Delta y_3 = -\Delta y$ for node 3, $\Delta x_4 = 0$ and $\Delta y_4 = \Delta y$ for node 4. Then in the traditional FDM, the second-order difference expressions of the spatial derivatives of the unknown function at node 0 are

$$\begin{aligned} u_{xx,0} &= \frac{u_1 + u_2 - 2u_0}{\Delta x^2} + O(\Delta x^2), \quad u_{yy,0} = \frac{u_3 + u_4 - 2u_0}{\Delta y^2} + O(\Delta y^2), \quad u_{x,0} = \frac{u_2 - u_1}{2\Delta x} + O(\Delta x^2), \\ u_{y,0} &= \frac{u_4 - u_3}{2\Delta y} + O(\Delta y^2) \end{aligned} \quad (46)$$

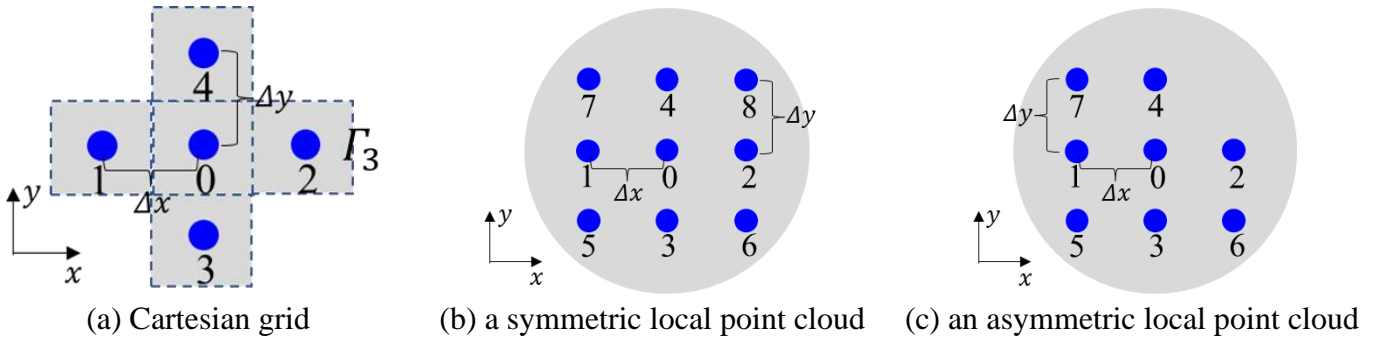


Fig. 4 Sketches of the Cartesian grid, a symmetric local point cloud, and an asymmetric local point cloud

For the generalized finite difference method (GFDM), Fu et al. [49] have proved the consistency of GFDM difference schemes. The key lies in the convergence order of GFDM. Firstly, according to the generalized difference expression derived by GFDM in Section 2.2 by ignoring the third-order and higher-order derivative terms of Taylor expansion, it can be inferred that the convergence order of GFDM is also less than or equal to 2. Here, the generalized difference expressions calculated based on two different local point clouds in Fig. 2 and Fig. 3 are given respectively, to show that the convergence order of GFDM is the second-order accuracy when the local point cloud symmetry is good. In the case of local point clouds with poor symmetry, it is generally only the first-order accuracy, which is the cost that the traditional FDM needs to pay when it is extended to GFDM in the case of arbitrary point clouds.

(i) Example 1: In the local point cloud shown in Fig. 4 (b), the central node is node 0. May as well suppose $\Delta x = \Delta y$, and take the radius of the influence domain of node 0 as $1.8\Delta x$, so there are other 8 nodes (i.e. from

node 1 to node 8) around node 0 in its influence domain.

Then, using the GFDM theory in Section 2.2, the generalized difference expressions of spatial derivatives at node 0 can be calculated. Taking u_{xx0} as an example, Eq. (47) can be obtained:

$$u_{xx0} \approx \sum_{j=1}^8 m_{3j} (u_j - u_0) \quad (47)$$

in which

$$(m_{31}, m_{32}, m_{33}, m_{34}, m_{35}, m_{36}, m_{37}, m_{38}) = \left(\frac{9.6308 \times 10^{-1}}{\Delta x^2}, \frac{9.6308 \times 10^{-1}}{\Delta x^2}, -\frac{3.6917 \times 10^{-2}}{\Delta x^2}, -\frac{3.6917 \times 10^{-2}}{\Delta x^2}, \frac{1.8459 \times 10^{-2}}{\Delta x^2}, \frac{2.4918 \times 10^{-2}}{\Delta x^2}, \frac{1.8459 \times 10^{-2}}{\Delta x^2}, \frac{1.8459 \times 10^{-2}}{\Delta x^2} \right) \quad (48)$$

According to Taylor's expansion of the unknown function at node 0, we can get:

$$\begin{aligned} u_1 &= u_0 - \Delta x u_{x0} + \frac{1}{2} \Delta x^2 u_{xx0} - \frac{1}{6} \Delta x^3 u_{xxx0} + O(r^4), \\ u_2 &= u_0 + \Delta x u_{x0} + \frac{1}{2} \Delta x^2 u_{xx0} + \frac{1}{6} \Delta x^3 u_{xxx0} + O(r^4), \\ u_3 &= u_0 - \Delta y u_{y0} + \frac{1}{2} \Delta y^2 u_{yy0} - \frac{1}{6} \Delta y^3 u_{yyy0} + O(r^4), \\ u_4 &= u_0 + \Delta y u_{y0} + \frac{1}{2} \Delta y^2 u_{yy0} + \frac{1}{6} \Delta y^3 u_{yyy0} + O(r^4), \\ u_5 &= u_0 - \Delta x u_{x0} - \Delta y u_{y0} + \frac{1}{2} \Delta x^2 u_{xx0} + \Delta x \Delta y u_{xy} + \frac{1}{2} \Delta y^2 u_{yy0} - \frac{1}{3!} \sum_{i=0}^3 C_3^i \Delta x^i \Delta y^{3-i} u_{x^i y^{3-i}} + O(r^4), \\ u_6 &= u_0 + \Delta x u_{x0} - \Delta y u_{y0} + \frac{1}{2} \Delta x^2 u_{xx0} - \Delta x \Delta y u_{xy} + \frac{1}{2} \Delta y^2 u_{yy0} + \frac{1}{3!} \sum_{i=0}^3 [(-1)^{3-i} C_3^i \Delta x^i \Delta y^{3-i} u_{x^i y^{3-i}}] + O(r^4), \\ u_7 &= u_0 - \Delta x u_{x0} + \Delta y u_{y0} + \frac{1}{2} \Delta x^2 u_{xx0} - \Delta x \Delta y u_{xy} + \frac{1}{2} \Delta y^2 u_{yy0} + \frac{1}{3!} \sum_{i=0}^3 [(-1)^i C_3^i \Delta x^i \Delta y^{3-i} u_{x^i y^{3-i}}] + O(r^4), \\ u_8 &= u_0 + \Delta x u_{x0} + \Delta y u_{y0} + \frac{1}{2} \Delta x^2 u_{xx0} + \Delta x \Delta y u_{xy} + \frac{1}{2} \Delta y^2 u_{yy0} + \frac{1}{3!} \sum_{i=0}^3 C_3^i \Delta x^i \Delta y^{3-i} u_{x^i y^{3-i}} + O(r^4) \end{aligned} \quad (49)$$

By introducing Eq. (48) and Eq. (49) into Eq. (47), Eq. (47) can be rewritten as:

$$\begin{aligned} \sum_{j=1}^8 m_{3j} (u_j - u_0) &= (m_{32} + m_{36} + m_{38} - m_{31} - m_{35} - m_{37}) \Delta x u_{x0} \\ &+ (m_{34} + m_{37} + m_{38} - m_{33} - m_{35} - m_{36}) \Delta y u_{y0} \\ &+ \frac{1}{2} (m_{31} + m_{32} + m_{35} + m_{36} + m_{37} + m_{38}) \Delta x^2 u_{xx0} \\ &+ \frac{1}{2} (m_{33} + m_{34} + m_{35} + m_{36} + m_{37} + m_{38}) \Delta y^2 u_{yy0} + O(r^4) \\ &= u_{xx0} + O(r^2) \end{aligned} \quad (50)$$

Then obtain:

$$u_{xx,0} = \sum_{j=1}^8 m_{3j} (u_j - u_0) + O(r^2) \quad (51)$$

Similarly, it is obtained that

$$u_{yy,0} = \sum_{j=1}^8 m_{4j} (u_j - u_0) + O(r^2) \quad (52)$$

For the first-order special derivative, the generalized difference expression of u_{x0} is

$$u_{x0} = \sum_{j=1}^8 m_{1j} (u_j - u_0) \quad (53)$$

where

$$(m_{11}, m_{12}, m_{13}, m_{14}, m_{15}, m_{16}, m_{17}, m_{18}) = \left(\frac{-0.4808}{\Delta x}, \frac{0.4808}{\Delta x}, 0, 0, \frac{-0.0096}{\Delta x}, \frac{0.0096}{\Delta x}, \frac{-0.0096}{\Delta x}, \frac{0.0096}{\Delta x} \right) \quad (54)$$

By introducing Eq. (49) and Eq. (54) into Eq. (53), Eq. (53) can be rewritten as:

$$\sum_{j=1}^8 m_{1j} (u_j - u_0) = u_{x0} + O(\Delta x^2) \quad (55)$$

As can be seen from Eqs. (51), (52), and (55), in the case of the local point cloud shown in Fig. 2, GFDM can have the same second-order accuracy as the traditional FDM for the first-order and second-order spatial derivatives.

(ii) Example 2: Remove node 8 in Fig. 4 (c) to form a local point cloud in Fig. 3 with poor symmetry. At this time, it can be calculated as follows:

$$\sum_{j=1}^7 m_{3j} (u_j - u_0) \quad (56)$$

in which

$$(m_{31}, m_{32}, m_{33}, m_{34}, m_{35}, m_{36}, m_{37}) = \left(\frac{9.6262 \times 10^{-1}}{\Delta x^2}, \frac{9.8754 \times 10^{-1}}{\Delta x^2}, -\frac{3.7377 \times 10^{-2}}{\Delta x^2}, -\frac{1.2459 \times 10^{-2}}{\Delta x^2}, \frac{2.4918 \times 10^{-2}}{\Delta x^2}, \frac{1.2459 \times 10^{-2}}{\Delta x^2}, \frac{1.2459 \times 10^{-2}}{\Delta x^2} \right) \quad (57)$$

Combining the Taylor expansion in Eq. (49), we can get:

$$\sum_{j=1}^7 m_{3j} (u_j - u_0) = u_{xx,0} + \frac{1}{3!} \frac{2.4918 \times 10^{-2}}{\Delta x^2} (3\Delta x^2 \Delta y u_{xxy,0} + 3\Delta x \Delta y^2 u_{xyy,0}) + O(r^2) \quad (58)$$

Since the Eq. (56) and Eq. (57) are obtained when $\Delta x = \Delta y$, rewrite the Eq. (58) as:

$$\sum_{j=1}^7 m_{3j} (u_j - u_0) = u_{xx,0} + \frac{2.4918 \times 10^{-2}}{3!} \left(3\Delta y + 3 \frac{\Delta y}{\Delta x} \Delta y \right) + O(r^2) = u_{xx,0} + O(r) \quad (59)$$

It can be seen that the generalized difference expression in Eq. (59) has only first-order accuracy, not second-order accuracy. Similarly, for the first-order spatial derivative, we can get:

$$u_{x0} = \sum_{j=1}^7 m_{1j} (u_j - u_0) \quad (60)$$

in which

$$(m_{11}, m_{12}, m_{13}, m_{14}, m_{15}, m_{16}, m_{17}) = \left(\frac{-4.8107 \times 10^{-1}}{\Delta x}, \frac{4.9353 \times 10^{-1}}{\Delta x}, \frac{-2.3880 \times 10^{-4}}{\Delta x}, \frac{1.2698 \times 10^{-2}}{\Delta x}, \frac{-6.2296 \times 10^{-3}}{\Delta x}, \frac{6.4684 \times 10^{-3}}{\Delta x}, \frac{-1.2698 \times 10^{-2}}{\Delta x} \right) \quad (61)$$

Then Eq. (62) is obtained. In the case of the local point cloud, the generalized difference expression of the first-order spatial derivative already contains the first-order term, but the coefficients of the first-order terms are small, which can be approximately regarded as having second-order accuracy.

$$\sum_{j=1}^8 m_{1j} (u_j - u_0) = u_{x0} - 3.4694 \times 10^{-18} u_{xx0} - 1.7347 \times 10^{-18} u_{xy0} + O(\Delta x^2) \quad (62)$$

The difference in the convergence order of the generalized difference expressions corresponding to the two local point clouds in Fig. 2 and Fig. 3 show that the convergence order of GFDM is less than or equal to that of the traditional low-order FDM, so GFDM is also a low-order method. When ignoring the influence of

the first-order upwind scheme on the convergence order of the discrete scheme, the FVM commonly used in reservoir numerical simulation has second-order accuracy for the diffusion term expressed by the second-order spatial derivative. It is a low-order FVM, which can be regarded as the integral form of the traditional low-order FDM to a certain extent. Of course, many high-order FVMs have been developed in computational fluid dynamics, but because the size of the reservoir calculation domain is relatively large, the grid size is generally about 10m or even larger, so high-order methods are rarely applied to reservoir numerical simulation. The proposed NCDMM is essentially an integral form of GFDM, which can be regarded as an extended finite volume method (EFVM). Therefore, NCDMM has the same approximation accuracy of diffusion term as GFDM, so that the convergence order of NCDMM is less than or equal to the second order.

3. Results of numerical analysis

In this section, several numerical test cases about reservoir numerical simulation are given to analyze the computational performances of the proposed NCDMM.

3.1 Two-phase porous flow in a rectangular heterogeneous domain

As mentioned above, injection and production wells exist in reservoir numerical simulation, and these wells are regarded as the point source or sink of the reservoir calculation domain. Therefore, this example compares the calculation results of this NCDMM with those of FVM commonly used in reservoir numerical simulation to illustrate that the proposed NCDMM can deal with the point source problem in reservoir numerical simulation with high accuracy in case of Cartesian or irregular point clouds. Fig. 5 (a) shows the strongly heterogeneous permeability profile. The size of the reservoir calculation domain in this example is $600\text{m} \times 180\text{m}$, and the thickness is 3m (Although this work focuses on the 2D problem, because the unit of the well flow rate in the reservoir flow problem is generally m^3/d , it is necessary to give the thickness of the reservoir model in the design of the numerical example, so that the strength of the source or sink term on the 2D domain can be obtained by dividing the well flow rate whose unit is m^3/d by the thickness), and the reservoir boundary is closed. In Fig. 5 (b), there are a production well and an injection well in the reservoir with constant flow rates of $60 \text{ m}^3/\text{d}$. Fig. 5 (c), (d), and (e) show the Cartesian mesh, Cartesian and irregular node collocations in the reservoir calculation domain respectively, in which the black solid points are the boundary and internal nodes of the calculation domain, The red diamond points are virtual nodes added to calculate the node control volumes and deal with the derivative boundary condition. In this example, for the collocations in Fig. 5 (d) and Fig. 5 (e), the radius of the node influence domain is selected as 10m, 15m, and 20m for calculation. Table 1 gives some physical parameters in this example, and Table. 2 shows the two-phase relative permeability data. Fig. 6 (a) and Fig. 6 (b) show the profiles of node control volumes (Not multiplied by the domain thickness) corresponding to the collocations in Fig. 5 (d) and Fig. 5 (e) respectively. It can be seen that for the Cartesian collocation in Fig. 5 (d) when the radius of the node influence domain is 10m, the control volume of the four corner nodes in the calculation domain is half of the control volume of the edge nodes and one-quarter of the control volume of the inner nodes. With the increase of the radius of the node influence region, the control area of each node will change accordingly. When the irregular collocation is used, the control volume of each node will also change accordingly. These results demonstrate the assertion in Eq. (23) in Section 2.2 that the node control area is a multivariate function of both the collocation in the calculation domain, but also the neighboring pairs between nodes. It also shows that the traditional mesh-based low-order FVM can be regarded as a special case of the proposed NCDMM under the small radius of node influence domain and regular (e.g. Cartesian) collocation.

Fig. 7 and Fig. 8 respectively show the calculated oil saturation and pressure profiles corresponding to the reference solution from the fine-mesh-based FVM simulation, FVM solution based on the Cartesian mesh in Fig. 5 (c), and NCDMM solution with different radii of the node influence domain in case of the Cartesian collocation in Fig. 5 (d). Fig. 9 shows the oil saturation profiles calculated by NCDMM with different radii of the node influence domain in case of the irregular collocation in Fig. 5 (e). It can be seen that the proposed NCDMM can obtain very similar calculation results to the traditional low-order FVM in both cases of Cartesian or irregular collocation, and can also be in good agreement with the reliable reference solution obtained from fine-mesh-based FVM. At the same time, different radii of the node influence domain have little impact on the calculation results. The results indicate that the proposed NCDMM can obtain sufficient accurate solutions under the condition of flexible collocation in the calculation domain and flexible selection of the radius of the node influence domain.

Table 3 shows the relevant parameters in the nonlinear solver set in all examples in this section. Fig. 10 shows the cumulative Newton iteration steps vs. the production time in the nonlinear solution process of

several cases. As seen from the figure, with the increase of the radius of the node influence domain, the consuming Newton iteration steps of the NCDMM will decrease, and all lower than those of the FVM. This shows that for the cases which both NCDMM and FVM can handle, NCDMM can achieve comparable computational efficiency to traditional low-order FVM.

The above comparisons of computational accuracy and efficiency between low-order FVM and the proposed NCDMM indicate the feasibility of forming an NCDMM-based general-purpose numerical simulator with strong robustness.

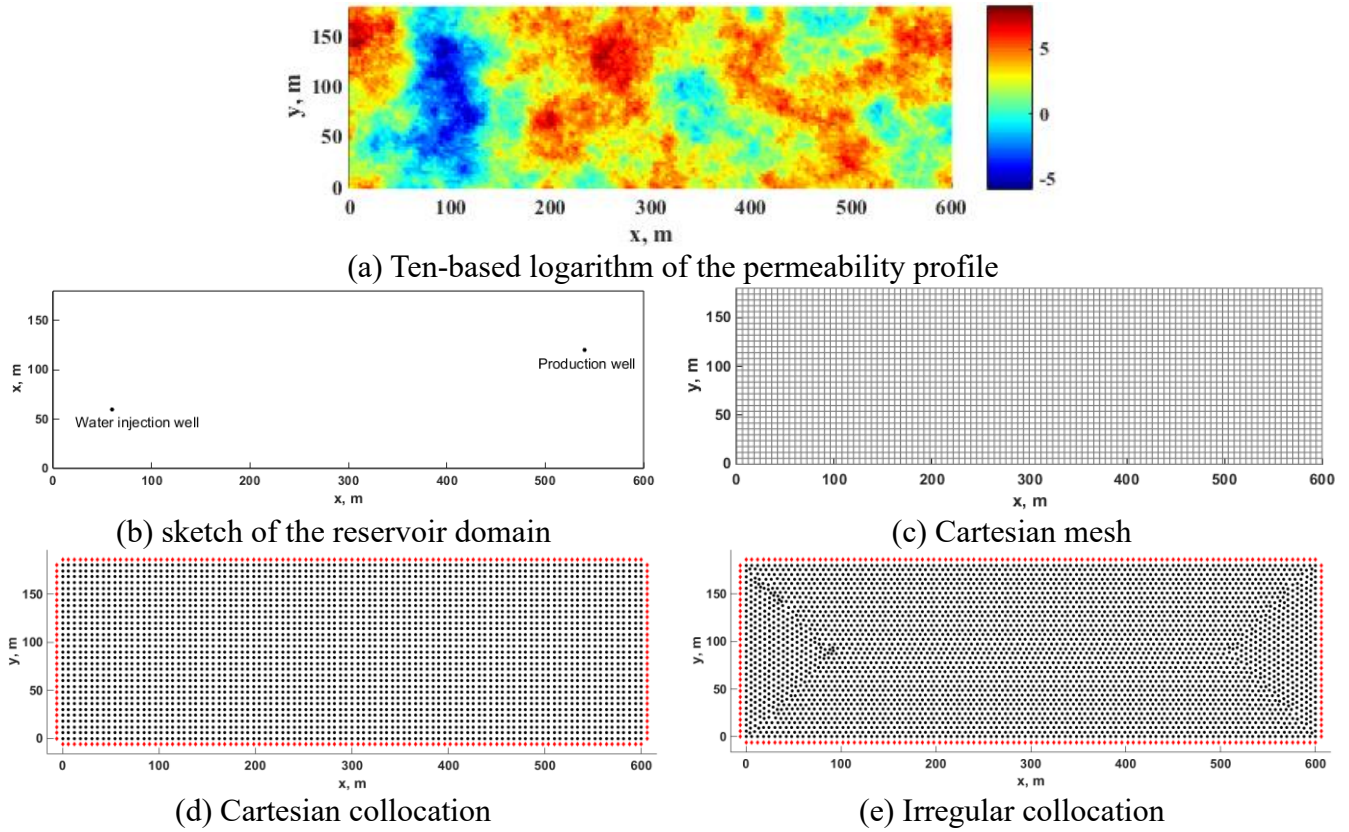
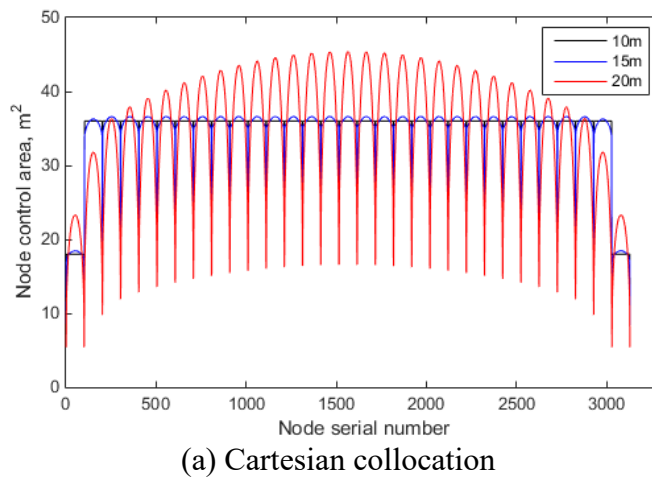
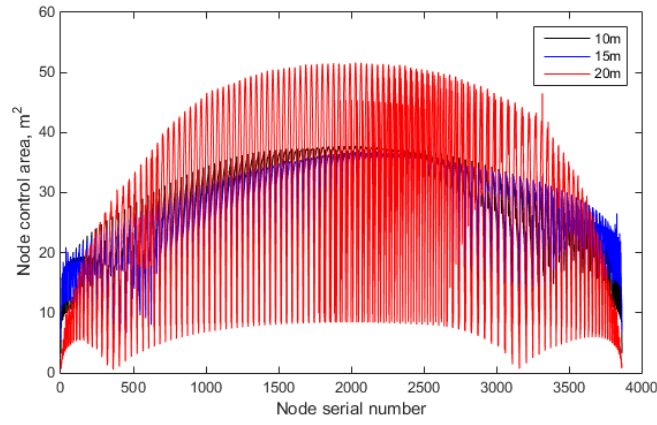


Fig. 5 sketches of the reservoir domain and various discretizations





(a) irregular collocation

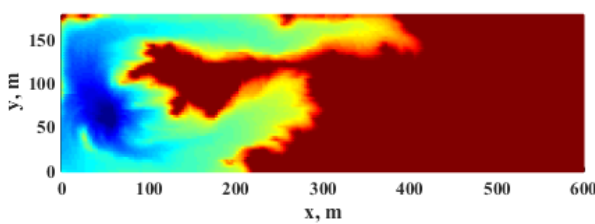
Fig. 6 Comparison of the node control areas in case of different radii of node influence domain

Table. 1 basic physical properties used in this numerical example

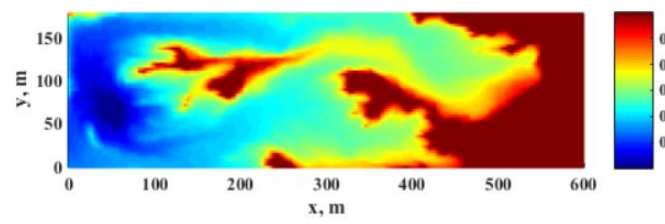
Properties	Values	Properties	Values
Porosity	0.2	Permeability	10 mD
Oil compressibility	$4 \times 10^{-4} \text{ MPa}^{-1}$	Water compressibility	$4 \times 10^{-4} \text{ MPa}^{-1}$
Rock compressibility	$2 \times 10^{-4} \text{ MPa}^{-1}$	Oil viscosity	2 mPa·s
Water viscosity	0.6 mPa·s	Initial reservoir pressure	15 MPa
Initial water saturation	0.20	Oil volume factor	1.0
Water volume factor	1.0	Reservoir thickness	3 m
Well radius	0.1 m	Skin factor	0

Table. 2 basic physical properties used in this numerical example

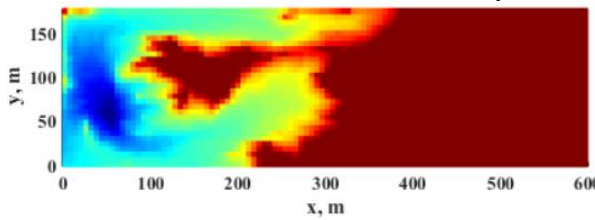
Sw	Krw	Kro	Sw	Krw	Kro
0.2	0	1	0.55	0.3403	0.1736
0.25	0.0069	0.8403	0.6	0.4444	0.1111
0.3	0.0278	0.6944	0.65	0.5625	0.0625
0.35	0.0625	0.5625	0.7	0.6944	0.0278
0.4	0.1111	0.4444	0.75	0.8403	0.0069
0.45	0.1736	0.3403	0.8	1	0
0.5	0.25	0.25			



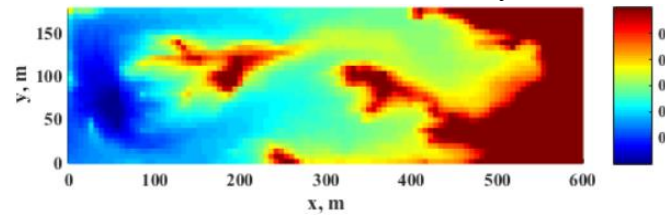
reference solution, 150 days



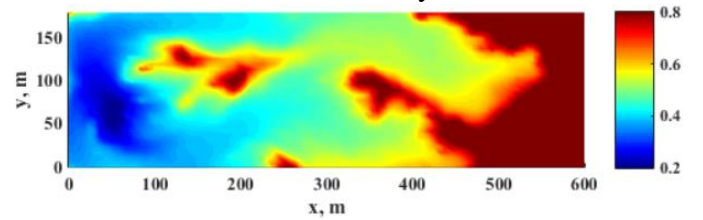
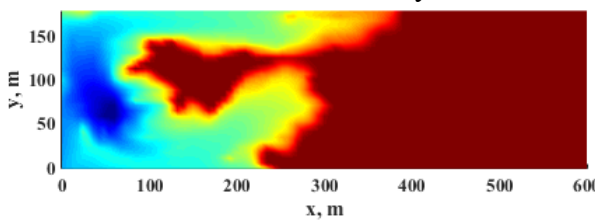
reference solution, 300 days



FVM, 150 days



FVM, 300 days



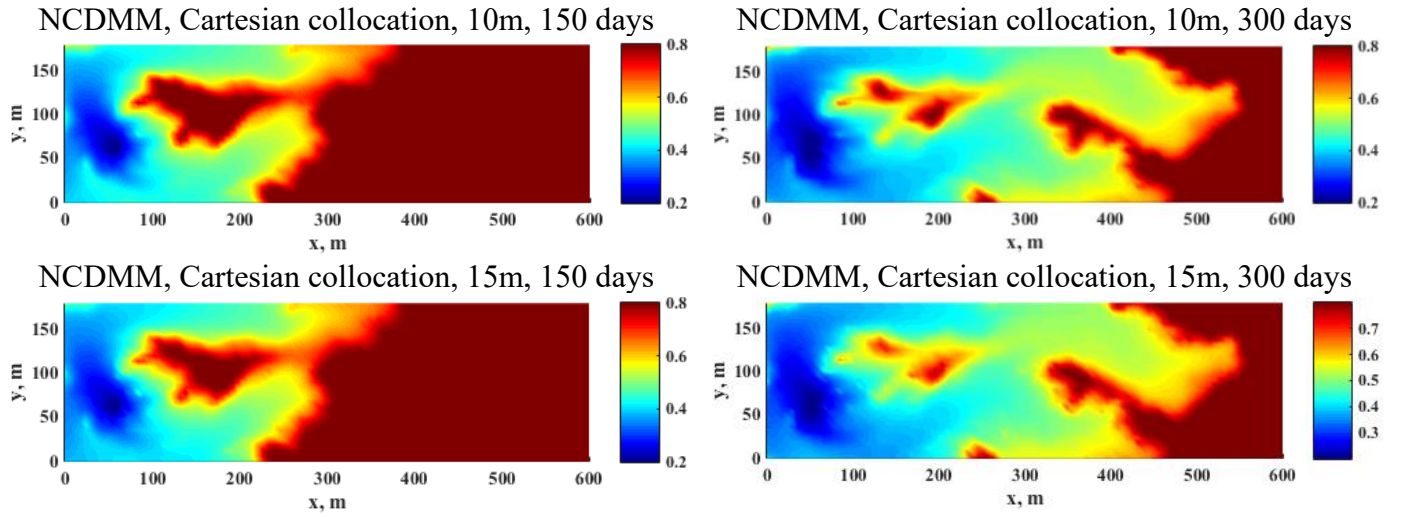


Fig. 7 oil saturation profiles calculated by FVM and NCDMM with different radii of node influence domain in case of Cartesian collocation

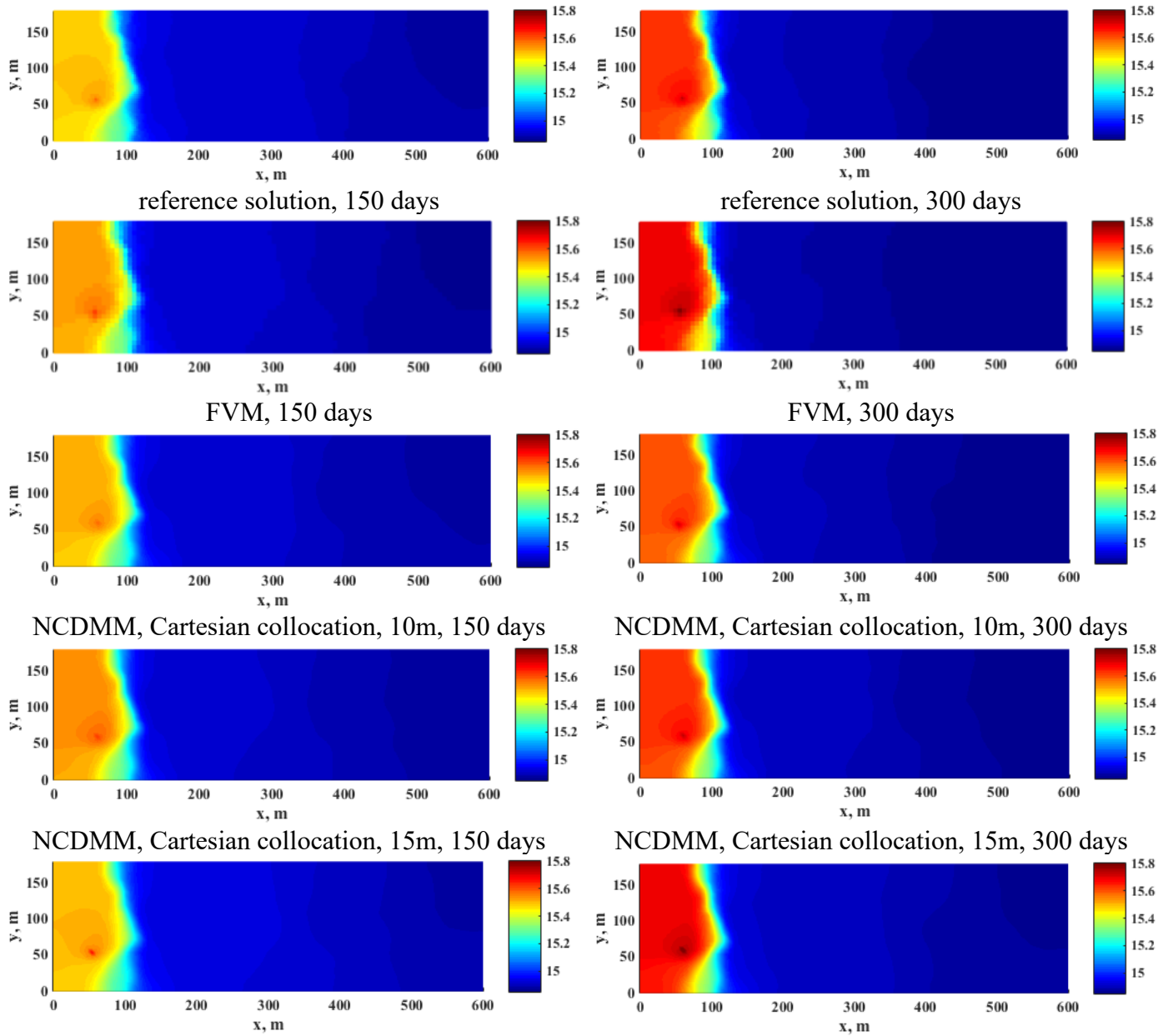


Fig. 8 pressure profiles calculated by FVM and NCDMM with different radii of node influence domain

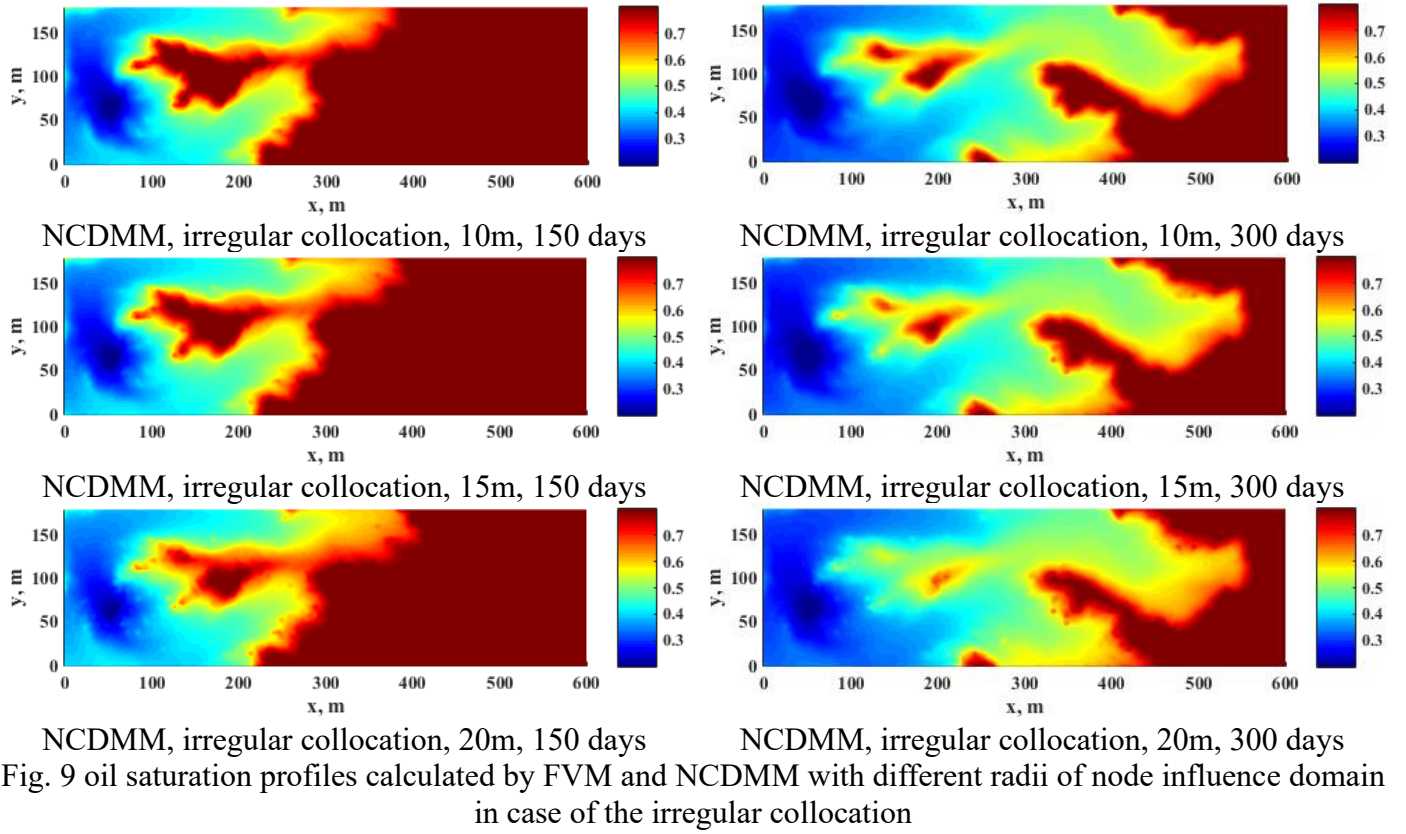
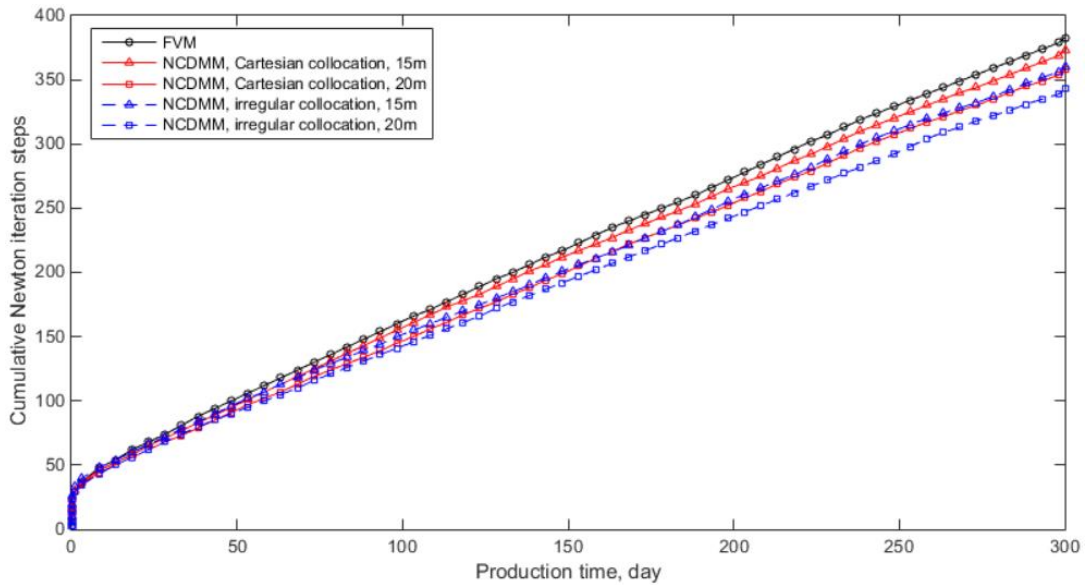


Table 3 Parameters in Newton nonlinear solver

Parameter	Value
Maximum time step size	5 days
Minimum time step size	0.001 day
Maximum Newton iterations	50
Error tolerance	10^{-6}
η_p	5 MPa
η_{s_w}	0.05



3.2 Two-phase porous flow with a polygonal boundary shape

In this section, the regular reservoir model is changed to the model with a polygonal closed boundary geometry in Fig. 11 (a). Permeability and other physical parameters are the same as those in Section 3.1. Fig. 11 (b) shows the meshless collocation of the reservoir calculation domain, and Fig. 11 (c) shows the node

control volume profiles calculated when the radius of the node influence domain are 10m, 15m, and 20m respectively. For such an irregular boundary shape, flexible meshless collocation is simpler than the conforming mesh. Based on the reservoir model in Section 3.1, we set the mesh permeability outside the boundary of the calculation domain in this example to zeros to obtain the fine mesh-based reference solution and the calculation results of traditional low-order FVM based on the Cartesian mesh.

Fig. 12 and Fig. 13 compare the water saturation and pressure profiles calculated by the proposed NCDMM under the different radius of the node influence domain with the reliable reference solution and the results from low-order FVM. It can be seen that the results of the NCDMM under different radii of the node influence domain are all very similar to the reference solution. Intuitively, the computational accuracy is slightly lower than that of the low-order FVM, but it is still acceptable. However, the proposed NCDMM can use flexible collocation to discretize the calculation domain with irregular boundary geometry, while low-order FVM depends on the complicated generation of conforming orthogonal mesh, or the method shown in this section of assigning zero permeability to the invalid cells outside the boundary in the case of rectangular Cartesian mesh, but this method is difficult to be generalized, and it will increase the actual cell number involved in the calculation and reduce the calculation efficiency. It can be seen that the proposed NCDMM is a novel meshless numerical method for porous flow simulation with sufficient calculation accuracy, good calculation performance, and flexible discretization of the calculation domain.

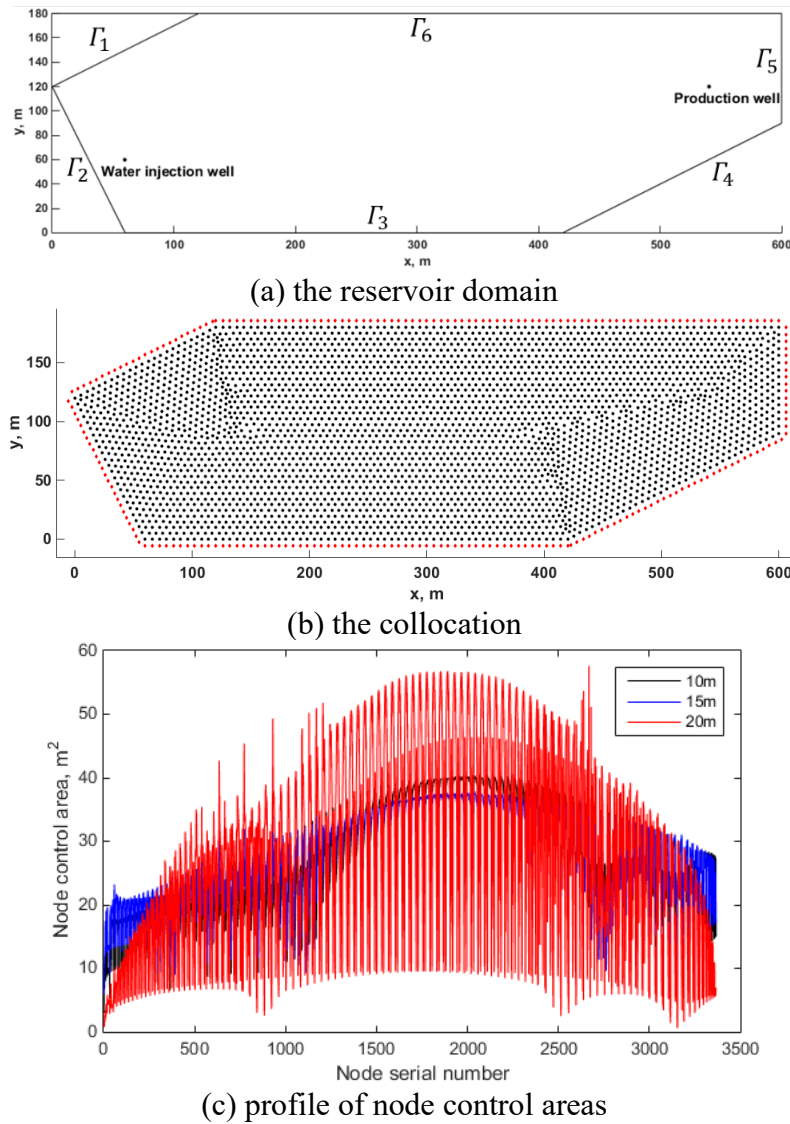


Fig. 11 sketches of some geometric information of the reservoir model

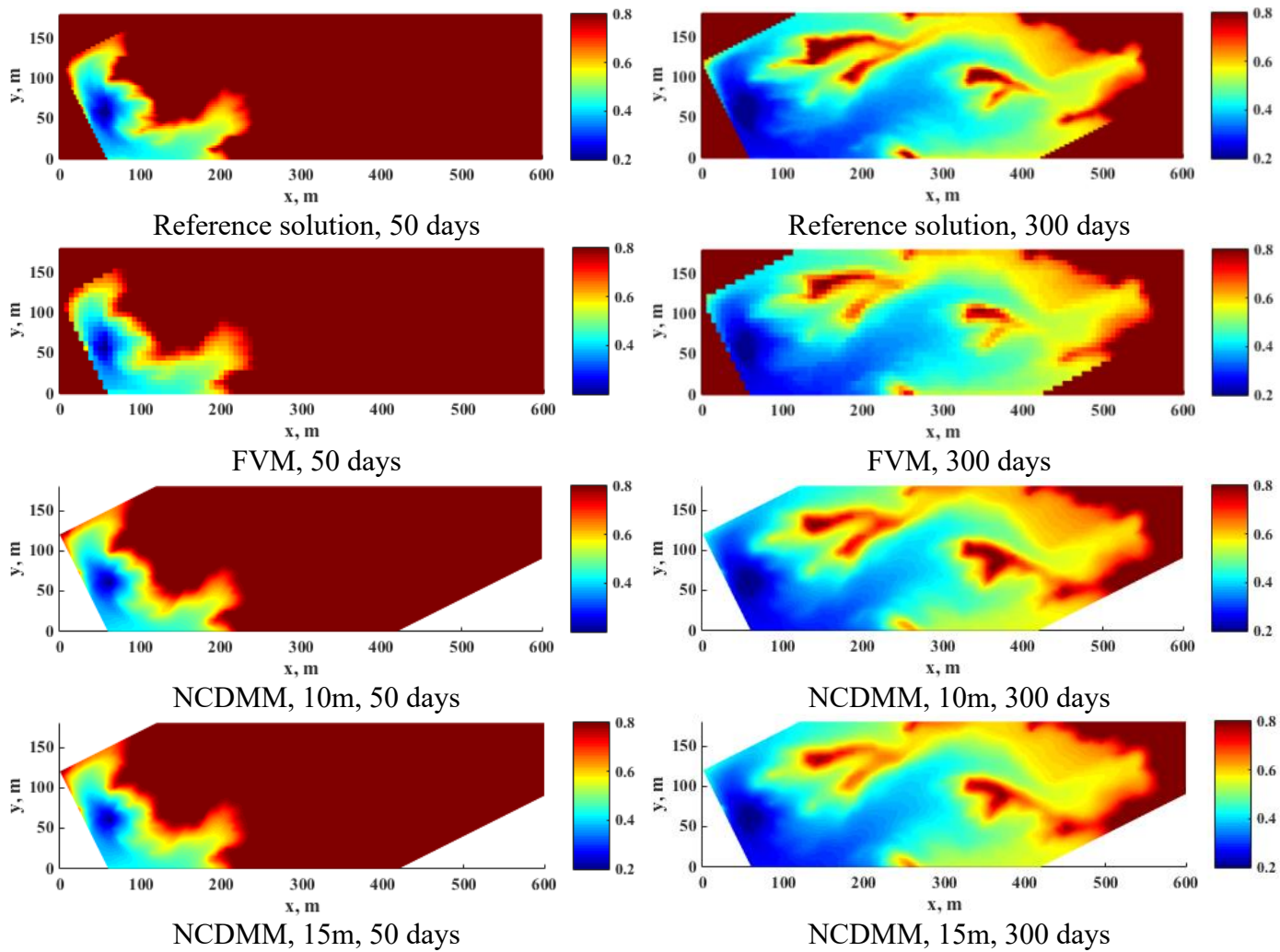
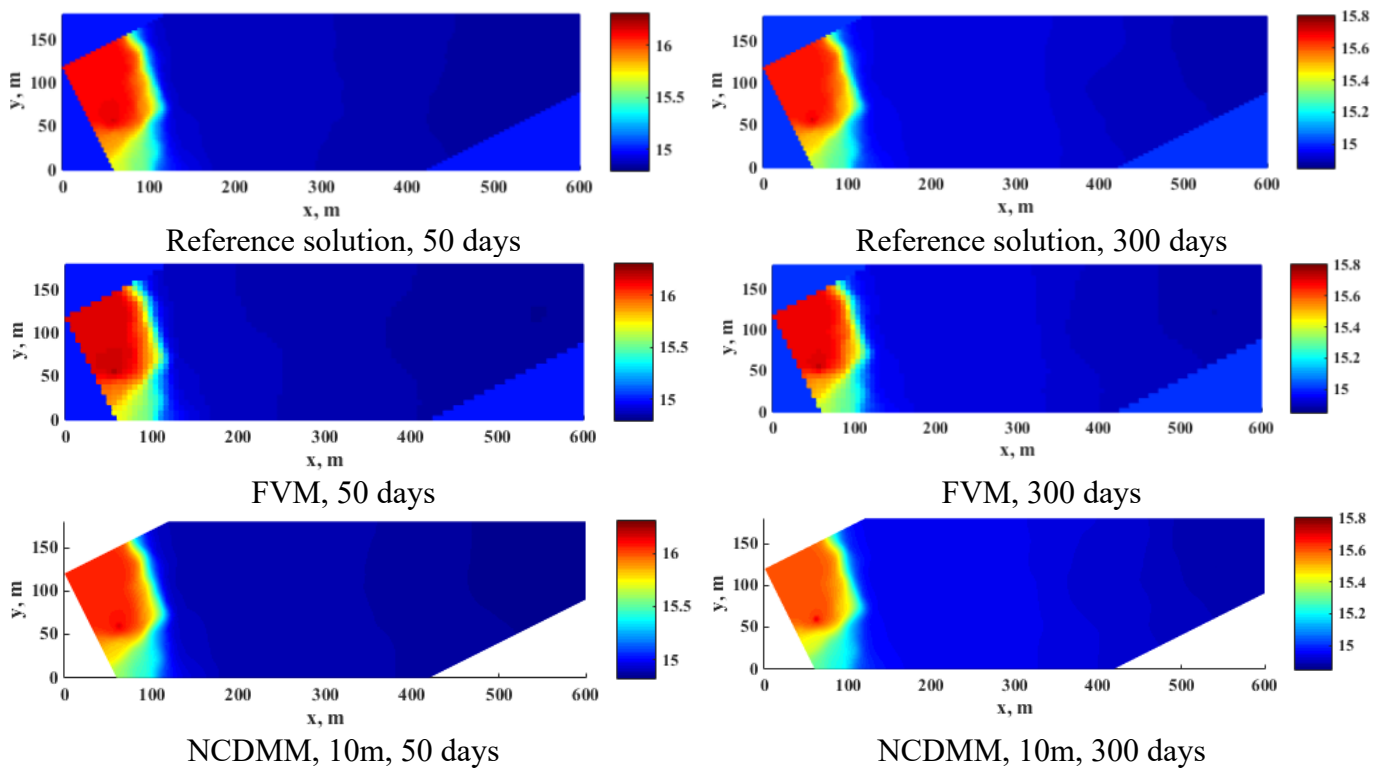


Fig. 12 oil saturation profiles calculated by low-order FVM and proposed NCDMM with different radii of the node influence domain



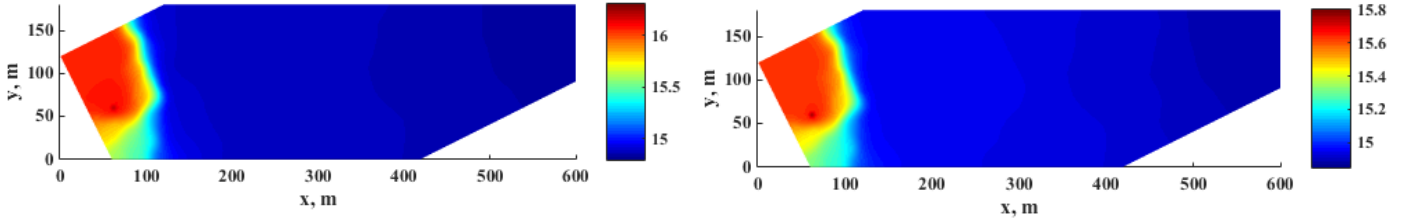


Fig. 13 pressure profiles calculated by low-order FVM and proposed NCDMM with different radii of the node influence domain

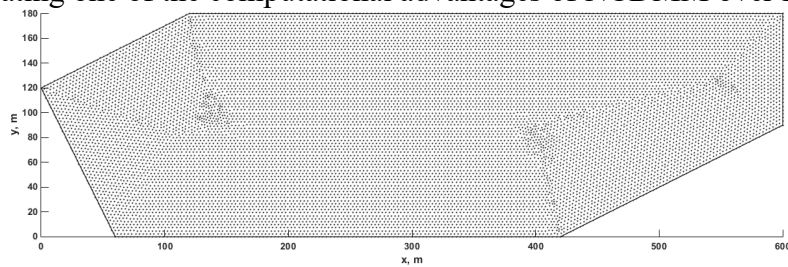
3.3 Two-phase porous flow with a Dirichlet boundary condition and a polygonal boundary shape

In this section, the reservoir geometric model, node collocations, and relevant physical properties in section 3.2 are still used, while the permeability is set as 100mD. There are two production wells in coordinates (200, 72), (420, 103) with a constant flowrate 60m³/d. The initial and boundary conditions are listed in Eq. (63) and Eq. (64) respectively, in which, the boundaries are at the Dirichlet boundary condition, indicating strong edge water. The initial water saturation is the irreducible water saturation.

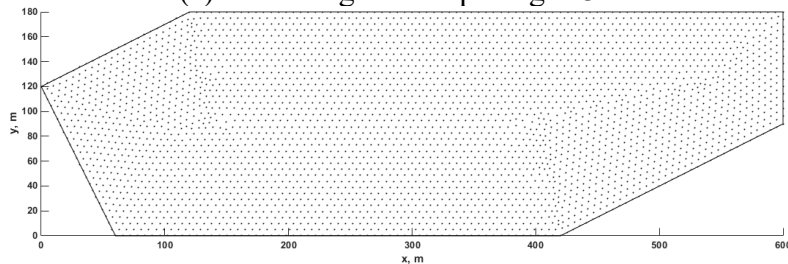
$$p|_{t=0} = 10\text{MPa}, \quad S_w|_{t=0} = 0.2 \quad (63)$$

$$p|_{\Gamma} = 10\text{MPa}, \quad S_w|_{\Gamma} = 0.8, \quad \Gamma = \Gamma_1 \cup \Gamma_2 \cup \Gamma_3 \cup \Gamma_4 \cup \Gamma_5 \cup \Gamma_6 \quad (64)$$

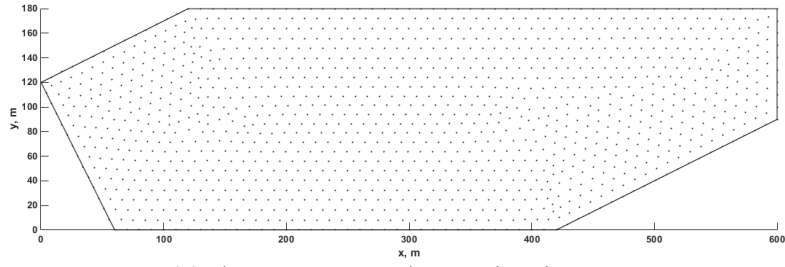
Fig. 14 shows the node collocations with different average node spacings (3m, 6m, 10m, and 15m) used in NCDMM for this example. Parameters of Newton nonlinear solver in Table 3 are employed. Fig. 15 and Fig. 16 compare the pressure and water saturation profiles at 100 days and 300 days calculated by NCDMM with the node collocations in Fig. 14. The FVM-based fine-mesh solution in a larger computational domain is used as the reference solution, in which, to impose the Dirichlet boundary condition in Eq. (64) when FVM is used, volume, pressure, and water saturation of the cells outside the real calculation domain are set as 10¹⁰m³, 10MPa, and 0.8 respectively, and the transmissibility between the cell outside the calculation domain and the cell inside the calculation domain is set large. Fig. 17 shows the relative errors versus the average node spacings. As seen from the comparisons of NCDMM results and FVM reference solutions, when the average node spacing becomes smaller, the NCDMM results gradually converge to the reference solution, and the corresponding computational error gradually decreases. Therefore, although the FVM can also deal with the Dirichlet boundary conditions, it is not straightforward enough and is more complicated to deal with in the case of complex boundary shapes. In contrast, NCDMM can handle Dirichlet boundary conditions very directly (including, of course, the Robin-type boundary conditions that are more difficult to handle directly with FVM), and the comparison of computational results shows that NCDMM achieves good computational performance, demonstrating one of the computational advantages of NCDMM over FVM.



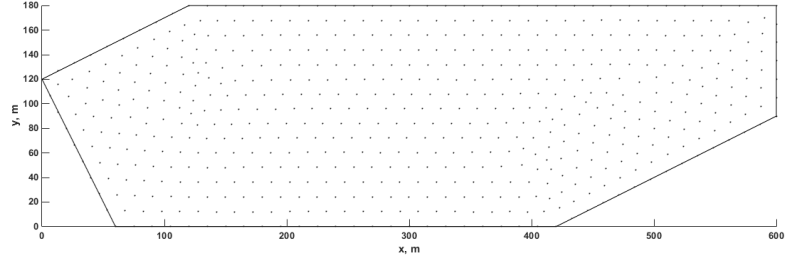
(a) the average node spacing is 3m



(b) the average node spacing is 6m



(c) the average node spacing is 10m



(d) the average node spacing is 15m

Fig. 14 the node collocations used in this example

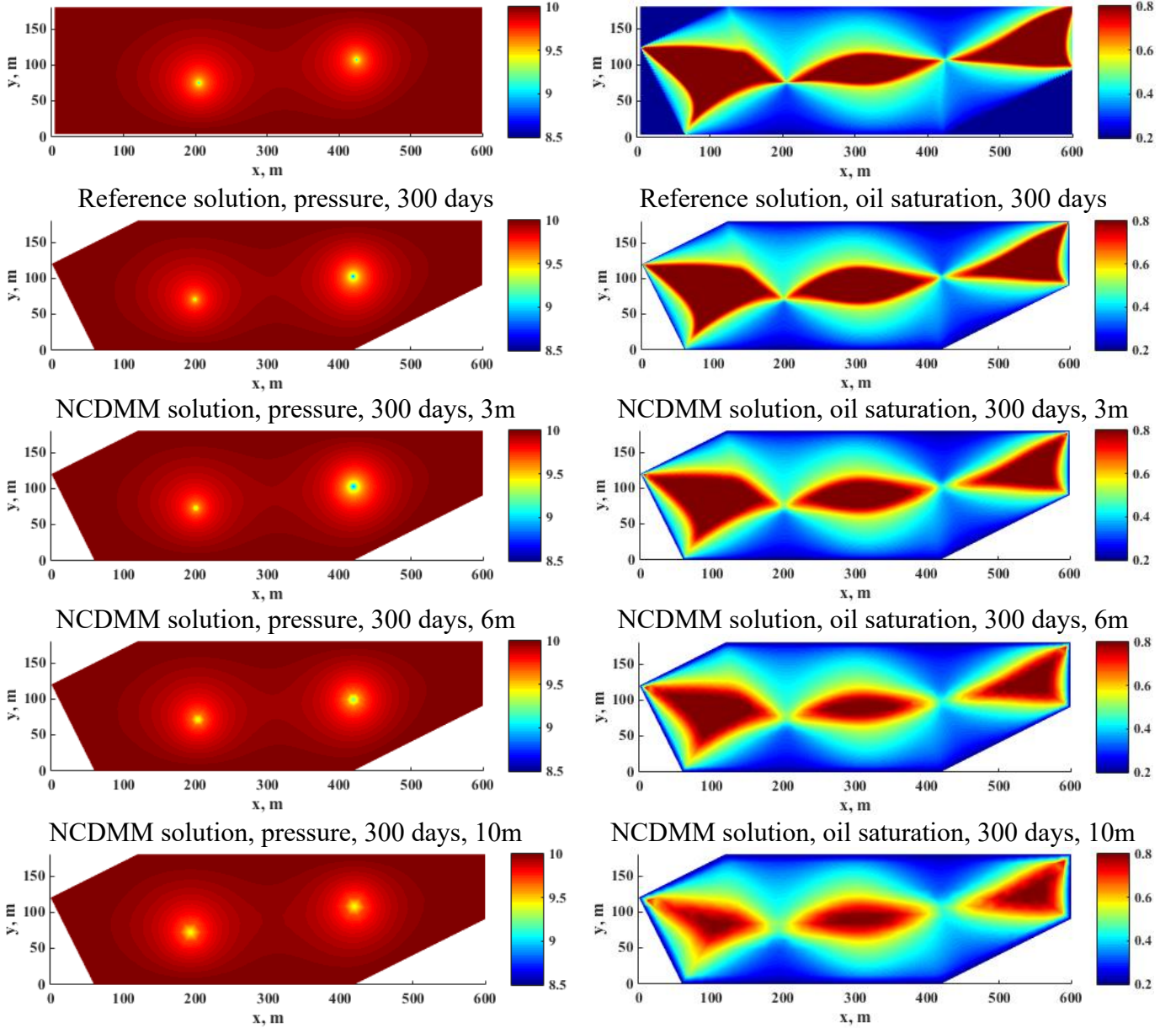


Fig. 15 Calculation results of FVM-based reference solution and proposed NCDMM with different average node spacings

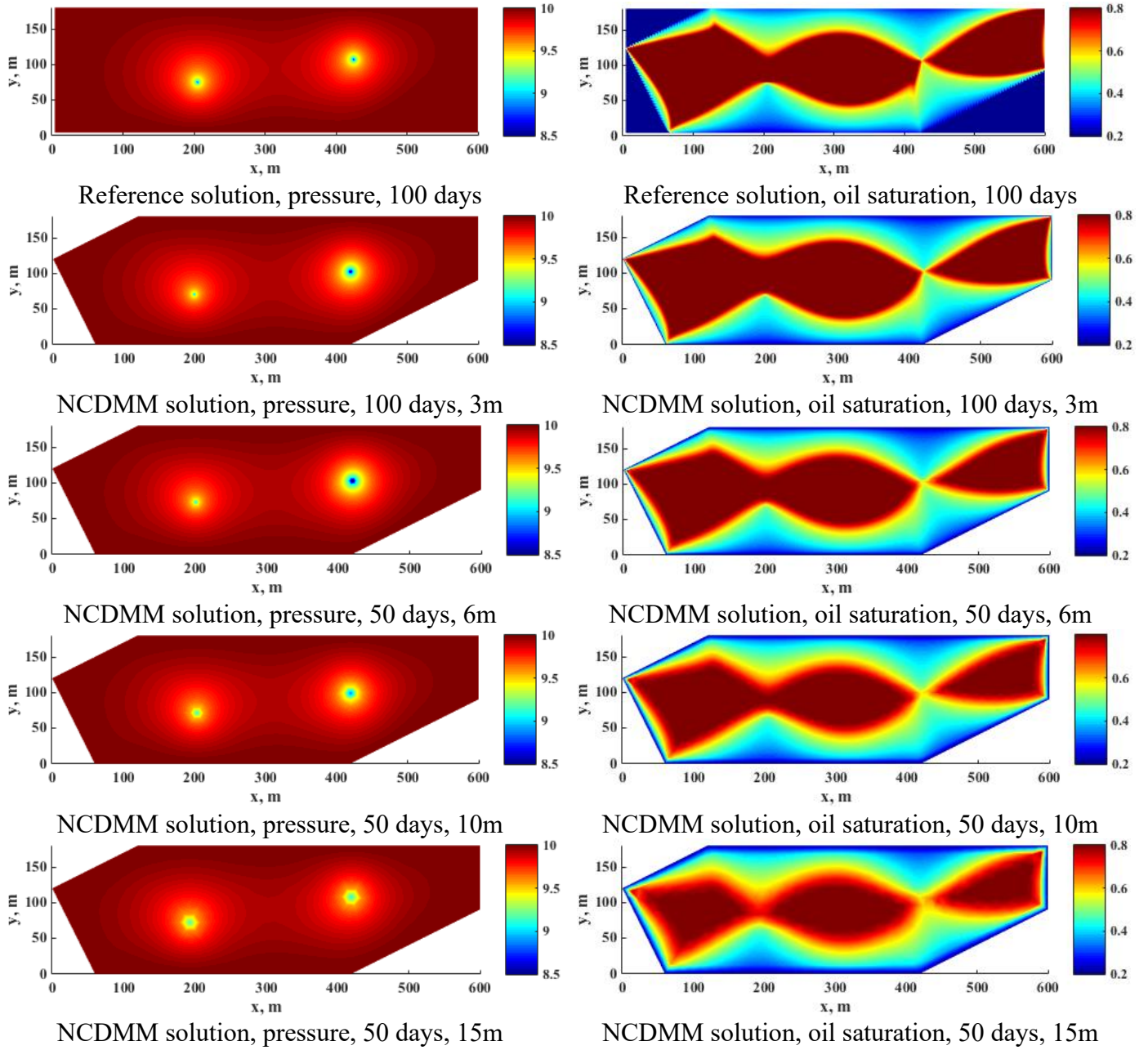


Fig. 16 Calculation results of FVM-based reference solution and proposed NCDMM with different average node spacings

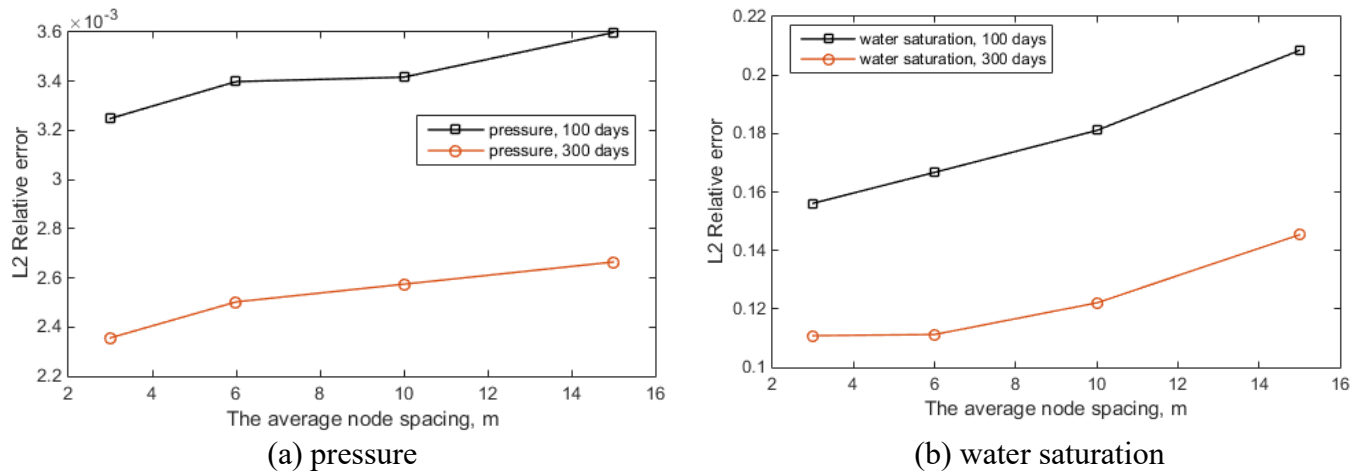


Fig. 17 the L_2 relative errors of calculated results

4. Conclusions

A novel meshless method based on the virtual construction of node control domains is developed, named NCDMM. Throughout the whole paper, five main conclusions can be obtained as follows:

- (1) Concepts of node control volume and connectable point cloud are defined in meshless GFDM, and the defined node control volumes are calculated by derived overdetermined linear equations when the point cloud of the computational domain is connectable. The virtual construction of node control domains means that NCDMM only cares about the volume of the node control domain, instead of the geometric shape of the node control domain.
- (2) The NCDMM discretization scheme of the governing equations is obtained by integrating the GFDM discretization scheme is integrated on the node control volume, which satisfies the local mass conservation.
- (3) The addition of virtual nodes is required for the treatment of derivative boundary conditions and the calculation of node control volumes.
- (4) Theoretically, compared with traditional low-order FVM commonly used in reservoir simulation, the proposed NCDMM can discretize the computational domain with complex geometry by a flexible meshless point cloud, instead of complicated mesh division. In addition, NCDMM can directly handle various boundary conditions. Take the porous flow problems in reservoir simulation as an example, the solution of the NCDMM-based discrete equations can directly employ the existing nonlinear solver in the FVM-based reservoir simulator, which significantly reduces the cost to construct an NCDMM-based general-purpose reservoir numerical simulator.
- (5) Three numerical examples are implemented to show the computational performances of the proposed NCDMM, and the results also verify the above theoretical advantages.

5. Future work

From our viewpoints, there may be four valuable future works:

- (1) Although we believe that there is not much technical difficulty in extending the NCDMM to 3D, it is still an interesting topic to extend the NCDMM to 3D and study its computational performances.
- (2) Considering the advantages of the NCDMM, the porous flow in the fractured reservoirs and fracture-vug-type reservoirs which have complex geometry and reservoirs with strong edge water and bottom water whose boundary conditions are not directly-handled closed boundaries may be the ideal potential application scenarios of NCDMM.
- (3) NCDMM is expected to be applied to more scientific and engineering fields.

6. Acknowledgements

Dr. Rao thanks the support from the National Natural Science Foundation of China (No. 52104017), the Open Fund of Cooperative Innovation Center of Unconventional Oil and Gas (Ministry of Education & Hubei Province) (No. UOG2022-14), and the Open Fund of Hubei Key Laboratory of Drilling and Production Engineering for Oil and Gas (Yangtze University) (Grant No. YQZC202201)

7. References

- [1] Benito, J. J., Urena, F., & Gavete, L. . (2001). Influence of several factors in the generalized finite difference method. *Applied Mathematical Modelling*, 25(12), 1039-1053.
- [2] Benito, J. J., Urea, F., Gavete, L., & Alvarez, R. . (2003). An h-adaptive method in the generalized finite differences. *Computer Methods in Applied Mechanics and Engineering*, 192(5), 735-759.
- [3] Gavete, L., Gavete, M. L., & Benito, J. J. . (2003). Improvements of generalized finite difference method and comparison with other meshless method. *Applied Mathematical Modelling*, 27(10), 831-847.
- [4] Benito, J. J., Ureña, F., Gavete, L., Salet, E., & Ureña, M. (2017). Implementations with generalized finite differences of the displacements and velocity-stress formulations of seismic wave propagation problem. *Applied Mathematical Modelling*, 52, 1-14.
- [5] Fan, C. M., & Li, P. W. . (2014). Generalized finite difference method for solving two-dimensional burgers' equations. *Procedia Engineering*, 79, 55-60.
- [6] Li, P. W. (2021). Space-time generalized finite difference nonlinear model for solving unsteady Burgers' equations. *Applied Mathematics Letters*, 114, 106896.
- [7] Li, P. W., & Fan, C. M. . (2017). Generalized finite difference method for two-dimensional shallow water equations. *Engineering Analysis with Boundary Elements*, 80(jul.), 58-71.
- [8] Li, P. W., Fan, C. M., & Grabski, J. K. (2021). A meshless generalized finite difference method for solving shallow water equations with the flux limiter technique. *Engineering Analysis with Boundary Elements*, 131, 159-173.
- [9] Ureña, F., Salet, E., Benito, J. J., & Gavete, L. (2012). Solving third-and fourth-order partial differential equations using GFDM: application to solve problems of plates. *International Journal of Computer Mathematics*, 89(3), 366-376.
- [10] Qu, W., & He, H. . (2020). A spatial-temporal gfdm with an additional condition for transient heat conduction analysis of fgms. *Applied Mathematics Letters*, 110, 106579.
- [11] Gu, Y., Wang, L., Chen, W., Zhang, C., & He, X. . (2017). Application of the meshless generalized finite difference

- method to inverse heat source problems. *International Journal of Heat and Mass Transfer*, 108, 721-729.
- [12] Xia, H., & Gu, Y. (2021). Generalized finite difference method for electroelastic analysis of three-dimensional piezoelectric structures. *Applied Mathematics Letters*, 117, 107084.
 - [13] Wang, Y., Yan, G., Fan, C. M., Wen, C., & Zhang, C. (2018). Domain-decomposition generalized finite difference method for stress analysis in multi-layered elastic materials. *Engineering Analysis with Boundary Elements*, 94(SEP), 94-102.
 - [14] Gu, Y., Qu, W., Chen, W., Song, L., & Zhang, C. (2019). The generalized finite difference method for long-time dynamic modeling of three-dimensional coupled thermoelasticity problems. *Journal of Computational Physics*, 384, 42-59.
 - [15] Fu, Z. J., Xie, Z. Y., Ji, S. Y., Tsai, C. C., & Li, A. L. (2020). Meshless generalized finite difference method for water wave interactions with multiple-bottom-seated-cylinder-array structures. *Ocean Engineering*, 195, 106736.
 - [16] Ostermann, I., Kuhnert, J., Kolymbas, D., Chen, C. H., Polymerou, I., Šmilauer, V., ... & Chen, D. (2013). Meshfree generalized finite difference methods in soil mechanics—part I: theory. *GEM-International Journal on Geomathematics*, 4(2), 167-184.
 - [17] Michel, I., Bathaeian, S. M. I., Kuhnert, J., Kolymbas, D., Chen, C. H., Polymerou, I., ... & Becker, A. (2017). Meshfree generalized finite difference methods in soil mechanics—part ii: numerical results. *GEM-International Journal on Geomathematics*, 8(2), 191-217.
 - [18] Cheng, M., & Liu, G. R. (2002). A novel finite point method for flow simulation. *International Journal for Numerical Methods in Fluids*, 39(12), 1161-1178.
 - [19] Chen, S. Y., Hsu, K. C., & Fan, C. M. (2021). Improvement of generalized finite difference method for stochastic subsurface flow modeling. *Journal of Computational Physics*, 429, 110002.
 - [20] Saucedo-Zendejo, F. R., Reséndiz-Flores, E. O., & Kuhnert, J. (2019). Three-dimensional flow prediction in mould filling processes using a GFDM. *Computational Particle Mechanics*, 6(3), 411-425.
 - [21] Suchde, P., Kuhnert, J., & Tiwari, S. (2018). On meshfree GFDM solvers for the incompressible Navier–Stokes equations. *Computers & Fluids*, 165, 1-12.
 - [22] Suchde, P., Kuhnert, J., Schröder, S., & Klar, A. (2017). A flux conserving meshfree method for conservation laws. *International Journal for Numerical Methods in Engineering*, 112(3), 238-256.
 - [23] Suchde, P., Kraus, H., Bock-Marbach, B., & Kuhnert, J. (2022). Meshfree One-Fluid Modelling of Liquid-Vapor Phase Transitions. *arXiv preprint arXiv:2203.10383*.
 - [24] Fu, Z. J., Tang, Z. C., Zhao, H. T., Li, P. W., Rabczuk, T. (2019). Numerical solutions of the coupled unsteady nonlinear convection–diffusion equations based on generalized finite difference method, *Eur. Phys. J. Plus* 134 (6), 272.
 - [25] Gu, Y., & Sun, H. (2020). A meshless method for solving three-dimensional time fractional diffusion equation with variable-order derivatives. *Applied Mathematical Modelling*, 78, 539-549.
 - [26] Kraus, H., Kuhnert, J., Meister, A., & Suchde, P. (2022). Meshfree Collocation for Elliptic Problems with Discontinuous Coefficients. *arXiv preprint arXiv:2204.05191*.
 - [27] Rao, X. (2022). An upwind general finite difference method (GFDM) for meshless analysis of heat and mass transfer in porous media. *Computational Particle Mechanics*.
 - [28] Rao, X., Liu, Y., & Zhao, H. (2022). An upwind generalized finite difference method for meshless solution of two-phase porous flow equations. *Engineering Analysis with Boundary Elements*, 137, 105-118.
 - [29] Edwards, M. G. (2011). Multi - dimensional wave - oriented upwind schemes with reduced cross - wind diffusion for flow in porous media. *International journal for numerical methods in fluids*, 67(1), 33-57.
 - [30] Rao, X., Cheng, L., Cao, R., Jia, P., Liu, H., & Du, X. (2020). A modified projection-based embedded discrete fracture model (pEDFM) for practical and accurate numerical simulation of fractured reservoir. *Journal of Petroleum Science and Engineering*, 187, 106852.
 - [31] Ewing, R. E. (1983). The mathematics of reservoir simulation. *Frontiers in Applied Mathematics*, 1.
 - [32] Lee, & S., H. (1989). Analysis of productivity of inclined wells and its implication for finite-difference reservoir simulation. *SPE (Society of Petroleum Engineers) Product. Eng.; (United States)*, 4(02), 173-180.
 - [33] Slough, K. J., Sudicky, E. A., & Forsyth, P. A. (1999). Grid refinement for modeling multiphase flow in discretely fractured porous media. *Advances in Water Resources*, 23(3), 261-269.
 - [34] Young, L. (1981). A finite-element method for reservoir simulation. *Society of Petroleum Engineers Journal*, 21(1), 115-128.
 - [35] Noorishad, J., & Mehran, M. (1982). An upstream finite element method for solution of transient transport equation in fractured porous media. *Water Resources Research*, 18(3), 588-596.
 - [36] Hajibeygi, H., Bonfigli, G., Hesse, M. A., & Jenny, P. (2008). Iterative multiscale finite-volume method. *Journal of Computational Physics*, 227(19), 8604-8621.
 - [37] Rao, X., Xin, L., He, Y., Fang, X., Gong, R., Wang, F., ... & Dai, W. (2022). Numerical simulation of two-phase heat and mass transfer in fractured reservoirs based on projection-based embedded discrete fracture model (pEDFM). *Journal of Petroleum Science and Engineering*, 208, 109323.
 - [38] Ren, G., & Younis, R. M. (2021). An integrated numerical model for coupled poro-hydro-mechanics and fracture propagation using embedded meshes. *Computer Methods in Applied Mechanics and Engineering*, 376(1–4), 113606.
 - [39] Monteagudo, J. E. P., & Firoozabadi, A. (2004). Control-volume method for numerical simulation of two-phase immiscible flow in two- and three-dimensional discrete-fractured media. *Water Resources Research*, 40(7), 7405.
 - [40] Cao, H. (2002). *Development of Techniques for General Purpose Simulators*. (Doctoral dissertation, Stanford

University.).

- [41] Zhi, Y. W. , Horne, R. , & D Voskov. A Geothermal Reservoir Simulator with AD-GPRS.
- [42] Lie, K. A. , Krogstad, S. , Ligaarden, I. S. , Natvig, J. R. , Nilsen, H. M. , & Skaflestad, B. . (2012). Open-source matlab implementation of consistent discretisations on complex grids. *Computational Geosciences*, 16(2), 297-322.
- [43] Liu, G. R. , & Gu, Y. T. . (2005). *An Introduction to Meshfree Methods and Their Programming*.
- [44] Milewski, S. . (2012). Meshless finite difference method with higher order approximation—applications in mechanics. *Archives of Computational Methods in Engineering*, 19(1), 1-49.
- [45] Di Giammarco, P., Todini, E., & Lamberti, P. (1996). A conservative finite elements approach to overland flow: the control volume finite element formulation. *Journal of Hydrology*, 175(1-4), 267-291.
- [46] Fuhrmann, J., Linke, A., & Langmach, H. (2011). A numerical method for mass conservative coupling between fluid flow and solute transport. *Applied numerical mathematics*, 61(4), 530-553.
- [47] Chen, H., Kou, J., Sun, S., & Zhang, T. (2019). Fully mass-conservative IMPES schemes for incompressible two-phase flow in porous media. *Computer Methods in Applied Mechanics and Engineering*, 350, 641-663.
- [48] Rao, X., Cheng, L., Cao, R., Zhang, X., & Dai, D. (2019). A mimetic Green element method. *Engineering Analysis with Boundary Elements*, 99, 206-221.
- [49] Fu, Z. J., Li, A. L., Zhang, C., Fan, C. M., & Zhuang, X. Y. (2020). A localized meshless collocation method for bandgap calculation of anti-plane waves in 2D solid phononic crystals. *Engineering Analysis with Boundary Elements*, 119, 162-182.